LBL-10713
Preprint

Lawrence Berkeley Laboratory
UNIVERSITY OF CALIFORNIA

Submitted to IEEE Transactions on Biomedical Engineering

SINGLE-PHOTON EMISSION COMPUTED TOMOGRAPHY: COMPENSATION FOR CONSTANT ATTENUATION

Grant T. Gullberg and Thomas F. Budinger

June 1980

Prepared for the U.S. Department of Energy under Contract W-7405-ENG-48

DISCLAIMER

LBL-10713

SINGLE-PHOTON EMISSION COMPUTED TOMOGRAPHY: COMPENSATION FOR CONSTANT ATTENUATION

Grant T. Gullberg and Thomas F. Budinger

Lawrence Berkeley Laboratory
University of California
Berkeley, California 94720

June 1980

SINGLE-PHOTON EMISSION COMPUTED TOMOGRAPHY: COMPENSATION FOR CONSTANT ATTENUATION

Grant T. Gullberg and Thomas F. Budinger

Lawrence Berkeley Laboratory
University of California
Berkeley, California 94720

ABSTRACT

A back-projection of filtered projection (BKFIL) reconstruction algorithm is presented that is applicable to single-photon emission computed tomography (ECT) in the presence of a constant attenuating medium such as the brain. The filters used in TCT — comprised of a ramp multiplied by window functions — are modified so that the single-photon ECT filter is a function of the constant attenuation coefficient. The filters give good reconstruction results with sufficient angular and lateral sampling. With continuous samples the BKFIL algorithm has a point spread function that is the Hankel transform of the window function. The resolution and statistical properties of the filters are demonstrated by various simulations. Statistical formulas for the reconstructed image show that the square of the percent-root-mean square uncertainty (%RMS) of the reconstruction is inversely proportional to the total measured counts. The results indicate that constant attenuation can be compensated for in single-photon ECT by using an attenuation-dependent filter that reconstructs the transverse section reliably. Computer time requirements are two times that of conventional TCT or positron ECT and there is no increase in memory requirements.

TABLE OF CONTENTS

I. INTRODUCTION

There are important fundamental differences between the reconstruction problem for the determination of the location and intensity of emission sources and the problem of conventional x-ray transmission computed tomography (TCT) wherein the attenuation coefficient is sought. In TCT the source position as well as the source strength is precisely known from the geometry of the x-ray TCT device and from source strength measurements. The ratio of detected photons to the measured source strength for each position of a TCT scan gives the projection of attenuation coefficients. However, in emission computed tomography (ECT), there is no *a priori* knowledge of the source strength and position; indeed, it is the source strengths and distributions that are being sought in the ECT problem. The additional unknown needed to solve the problem is the attenuation coefficient distribution. The detected information from various angles in the ECT problem is represented as projections of the source strengths and distributions. The attenuated Radon transform A_μ [1],[2] maps the source distribution ρ into the projection p $(A_\mu:\rho \to p)$ where

$$p(\xi,\theta) = \int_{\mathbb{R}^2} \rho(\underset{\sim}{r}) \exp\left[-\int \mu(\underset{\sim}{r}')\delta(\xi - \langle \underset{\sim}{r}', \underset{\sim}{\theta} \rangle)\, d\underset{\sim}{r}'\right] \delta(\xi - \langle \underset{\sim}{r}, \underset{\sim}{\theta} \rangle)\, d\underset{\sim}{r} \quad , \quad \langle \underset{\sim}{r}', \underset{\sim}{\theta}^{\perp} \rangle \geqslant \langle \underset{\sim}{r}, \underset{\sim}{\theta}^{\perp} \rangle \tag{1}$$

$\underset{\sim}{r} = (x,y)$, $\underset{\sim}{\theta} = (-\sin\theta, \cos\theta)$ and $\underset{\sim}{\theta}^{\perp} = (\cos\theta, \sin\theta)$ as shown in Fig. 1. If μ is constant over a convex set, these projections can be modified so that they correspond to the projections

$$p(\xi,\theta) = \int_{\mathbb{R}^2} \rho(\underset{\sim}{r})\ e^{\mu\langle \underset{\sim}{\theta}^{\perp}, \underset{\sim}{r} \rangle}\ \delta\{\xi - \langle \underset{\sim}{\theta}, \underset{\sim}{r} \rangle\} d\underset{\sim}{r} \quad , \tag{2}$$

which define the mapping $A_\mu : \rho \rightarrow p$. For TCT, the exponential term disappears and the resultant projection operation is known as the Radon transform [3].

The object of ECT is to implement an inverse of the attenuated Radon transform. This paper will present methods of implementing the inverse for constant attenuation with emphasis on a rapid algorithm that is nearly as fast as the conventional convolution method [4],[5],[6],[7]. The general theory on which this paper is based is outlined below.

An approximation to the inverse attenuated Radon transform for constant attenuation coefficient can be implemented by a modification of the projection data with a special convolver which differs from the conventional convolution function for TCT in that the ECT convolution function is a function of the attenuation coefficient. The conventional reconstruction technique in TCT modifies projections by a ramp filter rolled off by a window function to reduce noise artifacts. The second step in TCT is to back-project the modified projections. The point spread function of this linear reconstruction method is given as:

$$h_0 = \mathcal{B}\{c_0\} \tag{3}$$

where $\mathcal{B}$ is the back-projection operator and c_0 is the convolution function. Thus, the reconstructed image is the convolution of the point spread function h_0 with the true image distribution

$$\hat{\rho} = h_0 ** \rho \quad . \tag{4}$$

The Fourier transform of the convolution function can be represented as a function of the frequency f and is equal to the product of the window

function w(f), and a ramp function |f|:

$$\tilde{c}_0(f) = |f|\, w_0(f) \quad . \tag{5}$$

The optimum window is a function of resolution and noise for TCT. For ECT, a special window can be derived based on the attenuation coefficient as well as resolution and noise. Thus, the reconstructed image in ECT can be represented as

$$\hat{\rho} = \mathcal{B}_\mu \{ \mathcal{F}_1^{-1} (\tilde{c}_\mu \tilde{p}) \} \tag{6}$$

where the filter $\tilde{c}_\mu$ is a function of attenuation coefficient, and the back-projection operator $\mathcal{B}_\mu$ operates on the function g and is defined as $\mathcal{B}_\mu : g \to b$ [8], where

$$b(\underset{\sim}{r}) = \int_0^{2\pi} g(\langle \underset{\sim}{r}, \underset{\sim}{\theta} \rangle, \theta)\, e^{-\mu \langle \underset{\sim}{r}, \underset{\sim}{\theta}^{\perp} \rangle}\, d\theta \quad . \tag{7}$$

The reconstruction method in (6) is known as the back-projection of the filtered projection algorithm (BKFIL) [7]. The reconstructed image is related to the true image as in (4) by the point spread function

$$h_\mu(r) = \mathcal{B}_\mu(c_\mu) \quad . \tag{8}$$

The determination of the appropriate filter function with its corresponding point spread function is the major theme of this paper. The filter function is comprised of a window and a ramp filter: $\tilde{c}_\mu = \mathcal{F}_1[c_\mu] = |f| w_\mu$. (See also [9].) These window functions are related to the point spread function by the Hankel transform

$$h_\mu(r) = 2\pi \int_0^\infty 2w_\mu([s^2 + \mu^2/4\pi^2]^{\frac{1}{2}})\, J_o(2\pi rs)ds \quad . \qquad (9)$$

The relationship between the point spread function and different window functions will be shown in detail. The overall objective is to derive window functions that, for a given constant attenuation coefficient magnitude, will provide maximum resolution with minimum noise amplification.

Previous analyses of the attenuation problem in emission computed tomography using single-photon data have been presented in [1],[2],[7]-[16]. Methods for positron tomography are simpler than those for single-photon tomography and are discussed elsewhere [11],[17]-[19].

This article first discusses the method of modifying the attenuated Radon transform to render it independent of detector geometry and attenuation distribution. The attenuated back-projection operator is presented and a mathematical derivation of the point spread function for the BKFIL algorithm is given using this back-projection operator. Next, the analytical formulas for various window, filter, and convolution functions are given, and the influence of the window function and the magnitude of the attenuation coefficient on noise and resolution is characterized. Then statistical formulas for the filtering methods are developed and simulations of the BKFIL algorithm are given for data with various noise characteristics.

II. THE MODIFIED PROJECTIONS

In this section we will derive the modified attenuated Radon transform in (2) from the general transform given in (1). The purpose of modifying the measured projection data is to enable one to derive a general method of reconstructing attenuated projection data. This modification applies to

any source distributed within a constant attenuator whose extent can be represented as a convex set.

Using the rotated coordinates (see Fig. 1):

$$\begin{aligned} x &= \zeta\cos\theta - \xi\sin\theta \\ y &= \zeta\sin\theta + \xi\cos\theta \end{aligned} \quad , \tag{10}$$

the equation in (1) which defines the attenuated Radon transform A_μ can be rewritten as

$$p(\xi,\theta) = \int_{-\infty}^{\infty} \rho(\zeta\cos\theta - \xi\sin\theta, \zeta\sin\theta + \xi\cos\theta)\, a(\zeta,\xi,\theta)d\zeta \quad , \tag{11}$$

where

$$a(\zeta,\xi,\theta) = \exp\left[-\int_{\zeta}^{\infty} \mu(\zeta'\cos\theta - \xi\sin\theta,\ \zeta'\sin\theta + \xi\cos\theta)\, d\zeta'\right] . \tag{12}$$

If μ is constant over the convex region Ω and zero elsewhere, as shown in Fig. 2, then the attenuation factor in (12) can be simplified:

$$a(\zeta,\xi,\theta) = \exp\left[-\int_{\zeta}^{\beta(\xi,\theta)} \mu d\zeta'\right] = e^{-\mu\beta(\xi,\theta)}\, e^{\mu\zeta} \quad . \tag{13}$$

If the source distribution ρ is zero outside Ω, then the projections in (11) are

$$p(\xi,\theta) = \int_{-\infty}^{\infty} \rho(\zeta\cos\theta - \xi\sin\theta,\zeta\sin\theta + \xi\cos\theta)\, e^{\mu\zeta}\, d\zeta\, e^{-\mu\beta(\xi,\theta)} . \tag{14}$$

Multiplying both sides of (14) by $e^{-\mu\beta(\xi,\theta)}$ modifies the measured projections $p(\xi,\theta)$ so that the modified projections $p(\xi,\theta)$ in (2) are obtained from p using

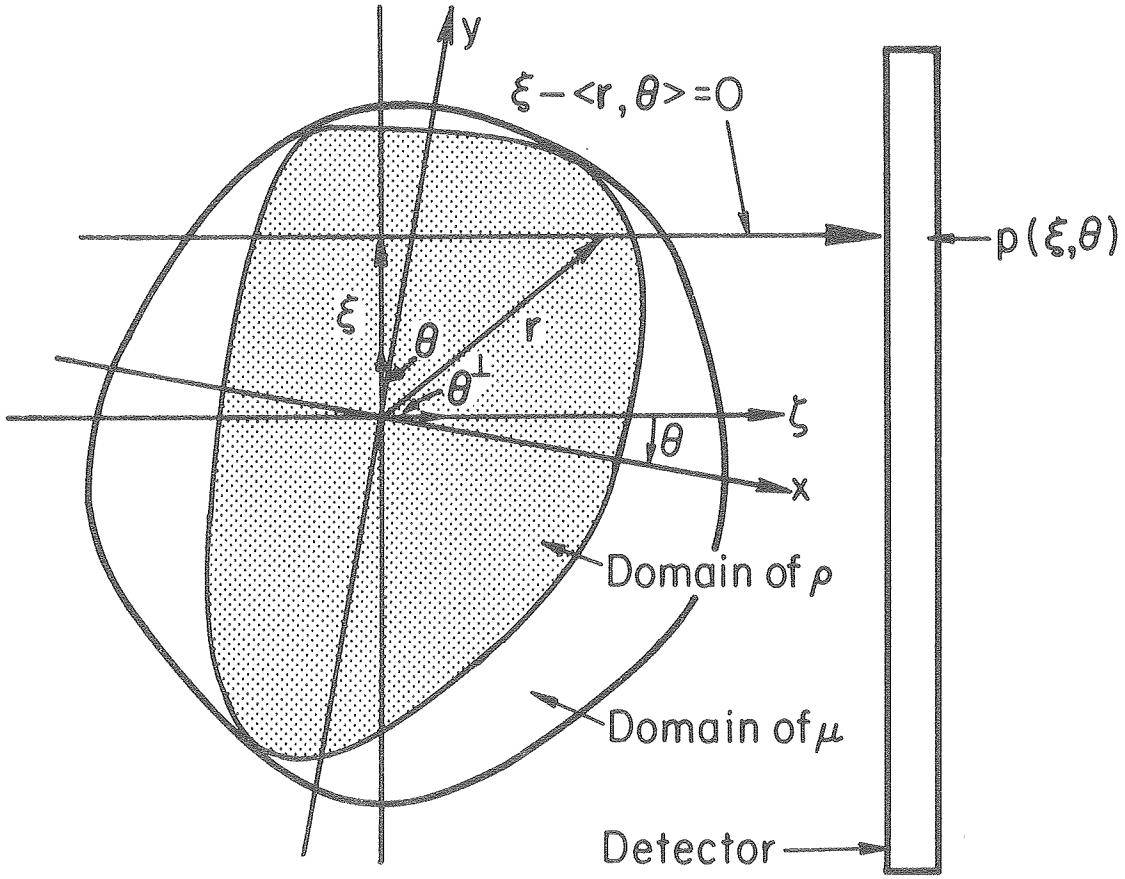

XBL803-3188

Fig. 1. Single-photon emission computed tomography. At the rotation angle θ and lateral sampling ξ, the detector will see those photons that travel along the line $\xi - \langle r, \theta \rangle = 0$ and are not attenuated by body tissue.

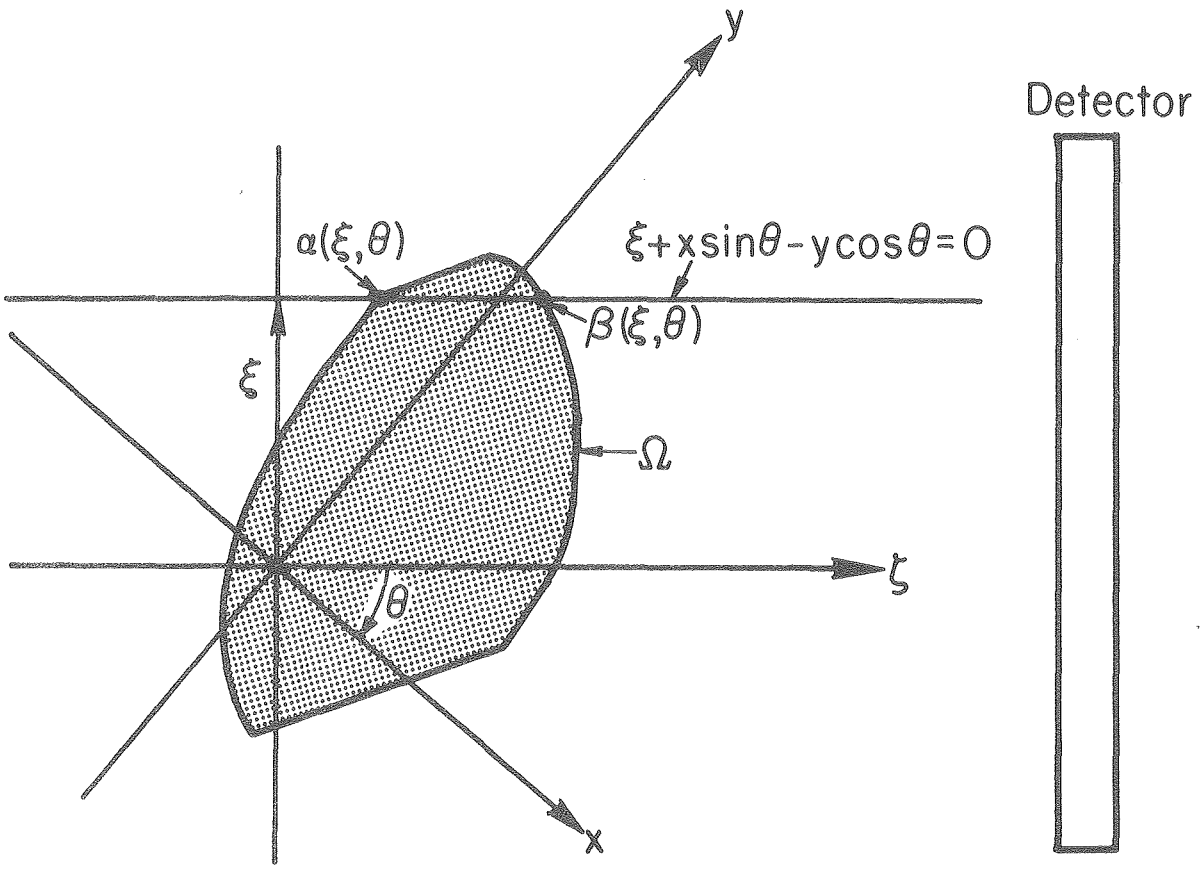

XBL803-3187

Fig. 2. Correction factor for the modified projections. If the attenuation coefficient μ is constant over the convex set Ω, then the measured projections $p(\xi,\theta)$ are modified to give $p(\xi,\theta) = e^{\mu\beta(\xi,\theta)}p(\xi,\theta)$ where $\beta(\xi,\theta)$ is the nearest point to the detector of the intersection of $\xi + x\sin\theta - y\cos\theta = 0$ and the set Ω.

$$p(\xi,\theta) = p(\xi,\theta)\, e^{\mu\beta(\xi,\theta)} = \int_{-\infty}^{\infty} \rho(\zeta\cos\theta - \xi\sin\theta, \zeta\sin\theta + \xi\cos\theta)\, e^{\mu\zeta}\, d\zeta \,. \tag{15}$$

This integral is equivalent to the integral in (2) and is another way of defining the mapping $A_\mu : \rho \to p$ for the constant attenuated Radon transform A_μ. If $p(\xi,\theta)$ are the measured projections, then the reconstruction algorithm BKFIL takes into account the fact that these projections have been modified by the factor $e^{\mu\beta(\xi,\theta)}$ before filtering and back-projecting. The point β, which can be positive or negative, is the intersection nearest the detector of the line $\xi + x\sin\theta - y\cos\theta = 0$ with the convex set Ω.

The modified transform A_μ has three important properties that simplify evaluation of (15). First, an integration is not required to evaluate the argument in the exponential factor; second, the integral in (15) is independent of detector location; and third, the integral in (15) is independent of the boundaries of the attenuator. One can think of the detector as being placed at the center of rotation in the coordinate system shown in Fig. 2. Photons emitted to the left of the central axis will be attenuated as usual with a reduction in the measured number, whereas photons emitted to the right of the central axis will be increased in number as if they were experiencing a negative attenuation coefficient.

III. THE ATTENUATED BACK-PROJECTION OPERATOR

An important aspect in the BKFIL algorithm of (6) is the attenuated back-projection operator $\mathcal{B}_\mu$ given in (7) which, by expanding the dot products, can be rewritten as

$$b(x,y) = \int_0^{2\pi} g(-x\sin\theta + y\cos\theta,\theta)\, e^{-\mu x\cos\theta - \mu y\sin\theta}\, d\theta \quad . \tag{16}$$

This operator assigns a value for the point (x,y) that is the summation of the projection values for all projection rays passing through the same point (x,y) weighted by the attenuation factor $e^{-\mu x\cos\theta - \mu y\sin\theta}$. In TCT the back-projection operator does not have this exponential factor and requires only integrating over π.

If the modified projections in (15) are back-projected before filtering, the result is an image equal to the true image convolved with a space-invariant kernel [2]:

$$(\mathcal{B}_\mu p)(x,y) = \rho(\underset{\sim}{r}) ** \frac{2}{\underset{\sim}{r}} \cosh(\mu \underset{\sim}{r}) \quad . \tag{17}$$

If $\mu = 0$ this back-projection image is just the true image convolved with $2/\underset{\sim}{r}$. This fact leads to an efficient Fourier filter algorithm that can deconvolve the back-projection image to obtain a reconstruction [20]-[22]. However, for single-photon ECT an algorithm cannot be devised since the back-projection image in (17) does not have a finite Fourier transform.

In the next section we will show how the attenuated back-projection operator leads to a description of the point spread function for the BKFIL algorithm.

IV. THE FILTER FUNCTION AND THE RESULTING POINT SPREAD FUNCTION

In the contemporary reconstruction process, a filter is applied to the frequency components of the projection data after which the data are inverse Fourier transformed and back-projected to form the image (BKFIL algorithm); or, equivalently, a convolver is applied to the projection data after which the result is back-projected. Two important convolution functions were developed by Ramachandran and Lakshminarayanan [5] and Shepp and Logan [6]. These methods of filtering the projection data are now used in most commercial x-ray scanners and positron emission tomographic systems because of their computational efficiency and because the filtering method requires very little computer memory. In this section we will show how the filtering method extends to single-photon ECT in the presence of a constant attenuation coefficient.

For constant attenuation the BKFIL algorithm gives the following reconstructed image:

$$\hat{\rho}(\underset{\sim}{r}) = [\mathcal{B}_\mu\{\mathcal{F}_1^{-1}(\tilde{c}_\mu \tilde{p})\}](\underset{\sim}{r}) = \int_0^{2\pi}\int_{-\infty}^{\infty} \tilde{c}(f)\, \tilde{p}(f,\theta)\, e^{2\pi i \langle \underset{\sim}{r},\underset{\sim}{\theta}\rangle}\, df\, e^{-\mu\langle \underset{\sim}{r},\underset{\sim}{\theta}^{\perp}\rangle}\, d\theta\,, \tag{18}$$

where $\hat{\rho}$ is the reconstructed distribution, $\tilde{c}(f)$ is a filter applied to the frequency components of the projection data $\tilde{p}$, and $\mathcal{F}_1^{-1}$ is the one-dimensional inverse Fourier transform. The equivalent implementation of (18) involves convolving the projection data with a configuration space convolver after which the back-projection operation is performed:

$$\hat{\rho}(\underset{\sim}{r}) = [\mathcal{B}_\mu(c_\mu * p)](\underset{\sim}{r}) = \int_0^{2\pi}\int_{-\infty}^{\infty} c_\mu(\langle \underset{\sim}{r},\underset{\sim}{\theta}\rangle - \xi)\, p(\xi,\theta)\, d\xi\, e^{-\mu\langle \underset{\sim}{r},\underset{\sim}{\theta}^{\perp}\rangle}\, d\theta\,. \tag{19}$$

The reconstructed image $\hat{\rho}$ in (18) and (19) represents the original image convolved with a point spread function $h_\mu(r)$ that is a function of the attenuation and filter shape [8]. To prove this, we substitute (2) into (19) to obtain the following expression for the estimated reconstruction:

$$\hat{\rho}(\underset{\sim}{r}) = \int_0^{2\pi}\int_{-\infty}^{\infty} c_\mu(\langle \underset{\sim}{r},\underset{\sim}{\theta}\rangle - \xi) \int_{\mathbb{R}^2} \rho(\underset{\sim}{r}')\, e^{\mu\langle \underset{\sim}{r}', \underset{\sim}{\theta}^\perp\rangle}\, \delta(\xi - \langle \underset{\sim}{r}', \underset{\sim}{\theta}\rangle) dr' \times e^{-\mu\langle \underset{\sim}{r}, \underset{\sim}{\theta}^\perp\rangle}\, d\xi\, d\theta \quad . \tag{20}$$

Assuming all functions are integrable, we can rearrange the order of integration; integrate first with respect to ξ to give

$$\hat{\rho}(\underset{\sim}{r}) = \int_{\mathbb{R}^2} \rho(\underset{\sim}{r}') \int_0^{2\pi} c_\mu(\langle \underset{\sim}{r}-\underset{\sim}{r}', \underset{\sim}{\theta}\rangle)\, e^{-\mu\langle \underset{\sim}{r}-\underset{\sim}{r}', \underset{\sim}{\theta}^\perp\rangle}\, d\theta\, d\underset{\sim}{r}' \quad . \tag{21}$$

If $h_\mu = \mathcal{B}_\mu\{c_\mu\}$, then this can be rewritten as

$$\hat{\rho}(\underset{\sim}{r}) = \int_{\mathbb{R}^2} \rho(\underset{\sim}{r}')\, h_\mu(\underset{\sim}{r} - \underset{\sim}{r}')\, d\underset{\sim}{r}' = (\rho ** h_\mu)(r) \quad . \tag{22}$$

Thus the reconstruction $\hat{\rho}$ is the convolution of the original image with a space invariant point spread function h_μ equal to the back-projection of the convolution function c_μ.

Ideally, we choose the convolution function c_μ so that its back-projection h_μ is a delta function. However, it is unrealistic and unnatural to force the solution to c_μ to be based on a perfect delta function response. In practical applications with a finite number of projections sampled at a finite number of points, the discrete back-projection of c_μ can only

approximate a delta function, and the function h_μ is referred to as the point spread function of the reconstruction procedure. Convolvers with point spread functions closely approximating a delta function give very good spatial resolution but tend to amplify statistical fluctuations in the data so that contrast resolution deteriorates.

If the point spread function is isotropic, for example, it may be represented as a Gaussian; then for continuous sampling, the convolution function c_μ is the solution to the integral equation

$$h_\mu(r) = \int_0^{2\pi} c_\mu(r\sin\theta)\, e^{-\mu r\cos\theta}\, d\theta \quad . \tag{23}$$

For $\mu = 0$, (23) is known as Schlomilch's integral equation [23], and if $h_0(r)$ has a continuous derivative, $c_0(\xi)$ is given by

$$c_0(\xi) = \frac{h_0(0)}{2\pi} + \frac{\xi}{2\pi}\int_0^{\pi/2} h_0'(\xi\sin\theta)\, d\theta \quad . \tag{24}$$

Tanaka and Iinuma [24] give an expression for c_0 when h_0 is a Gaussian point spread function. By using a least squares approach we solved (23) for various attenuation coefficients to give the convolution functions and corresponding filters shown in Fig. 3 [2]. Another method of solving (23) for the convolution function c_μ is to expand both h_μ and c_μ in a power series and equate their coefficients. This was done for a Gaussian point spread function in [2] and [25].

Our approach here is to characterize the filter as

$$\tilde{c}_\mu(f) = |f|\, w_\mu(f) \tag{25}$$

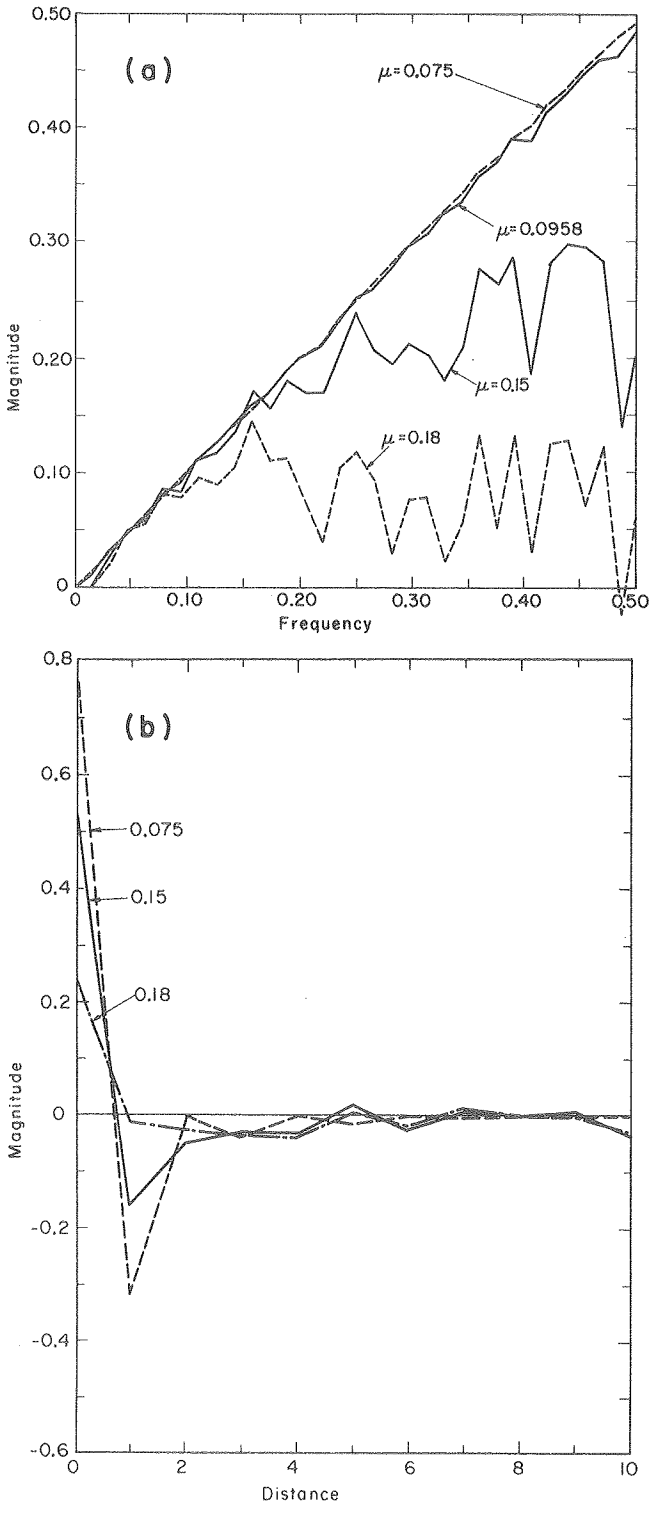

XBL803-3189

Fig. 3. Convolvers in (b) evaluated by a least-squares fit of (23) for μ = 0.075, 0.0958, 0.15, 0.18 (projection bin widths)$^{-1}$. The point response function h_μ was determined by back-projecting over 360° using (3) and $\mu = 0$, 360 equal projections of the Ramachandran and Lakshminarayanan convolver (36) into a 64×64 pixel array. In (a) are shown the filter functions that are the discrete Fourier transform of the convolvers in (b).

and relate the window function w_μ to the point spread function h_μ. Several classes of window functions have been applied to computed tomography: Butterworth [7], Hann and Hamming [7], [26], Parzen [7], Shepp and Logan [27], a cosine filter [28], a Wiener type (minimum mean squared error filter) [29], [30], and the rectangular window [7] which when applied to the basic ramp filter results in a sharp cut-off. These windows and their characteristics are well known in signal processing [e.g., see Refs. 31, 32]. The purpose of these windows applied to the basic ramp filter is to minimize the artifacts caused by noise in the projection data. The selection of a specific filter is based on some criterion (usually visual) of optimizing resolution and minimizing noise in the reconstruction image. In Section V we show that these filters can be modified to accommodate the presence of constant attenuation in single-photon ECT. For single-photon ECT, the noise propagation vs. resolution properties of the window function are complicated by the effects of attenuation. Thus the window functions must be designed not only to give a narrow central window to insure adequate resolution but also to minimize the effects of attenuation and noise.

In (22) we saw that the reconstructed image represents the original image convolved with a point spread function $h_\mu(r)$ that is a function of the attenuation and filter shape. Taking the inverse Fourier transform of (25) and substituting it into (23), we see that the point spread function can be expressed in terms of the window function $w_\mu(f)$:

$$h_\mu(r) = \int_0^{2\pi} \int_{-\infty}^{\infty} |f|\, w_\mu(f)\, e^{2\pi i f r \sin\theta}\, df\, e^{-\mu r \cos\theta}\, d\theta. \qquad (26)$$

Assuming that all functions are integrable, we rewrite (26) so that the first integration is with respect to θ:

$$h_\mu(r) = \int_{-\infty}^{\infty} |f|\, w_\mu(f) \int_0^{2\pi} e^{2\pi i f r \sin\theta - \mu r \cos\theta}\, d\theta\, df. \tag{27}$$

Integrating over θ gives [9]

$$h_\mu(r) = 2\pi \int_{-\infty}^{\infty} |f|\, w_\mu(f)\, J_o\left(2\pi r \sqrt{f^2 - \mu^2/4\pi^2}\right) df \tag{28}$$

where J_0 is the zeroth order Bessel function. If the window function is chosen so that $w(f)$ is zero for $|f| < \mu/2\pi$ and $w(-f) = w(f)$ for $|f| > \mu/2\pi$, we can rewrite (28):

$$h_\mu(r) = 2\pi \int_{\mu/2\pi}^{\infty} 2f\, w_\mu(f)\, J_o\left(2\pi r \sqrt{f^2 - \mu^2/4\pi^2}\right) df \quad . \tag{29}$$

Making the change of variables $s = \sqrt{f^2 - \mu^2/4\pi^2}$ gives

$$h_\mu(r) = 2\pi \int_0^{\infty} 2w_\mu\left([s^2 + \mu^2/4\pi^2]^{\frac{1}{2}}\right) J_o(2\pi r s)\, s\, ds \quad ,$$

$$= \mathcal{H}\{\, 2w_\mu([s^2 + \mu^2/4\pi^2]^{\frac{1}{2}}); r \,\} \quad . \tag{30}$$

where $\mathcal{H}$ is the Hankel transform [33].

V. WINDOW AND FILTER FUNCTIONS

The relationship between the integrable window function w and the point spread function h in (30) makes the following two assumptions:

$$\text{(i)} \qquad w_\mu(f) = 0 \quad , \quad |f| < \mu/2\pi \quad ,$$

$$\text{(ii)} \qquad w_\mu(-f) = w_\mu(f) \quad .$$

Assumption (i) correlates with the numerical results of the least-square fits in Fig. 3, where for $\mu = 0.15, 0.18$, the filters $\tilde{c}(f)$ $(=|f|w_\mu(f))$ bend away from the ramp function and approach zero at the low frequencies. The shapes of example window functions that we will describe are shown in Fig. 4. Besides having a minimum cut-off frequency of $\mu/2\pi$, they also have a maximum cut-off frequency $f_m = 0.5$. We will see that in addition to assumption (i), these windows differ from those in [11] in that the frequency has been replaced by $(f^2 - \mu^2/4\pi^2)^{\frac{1}{2}}$. We will also give a modification of the Shepp and Logan [27], Gaussian [9], and Butterworth [11] window functions.

The filters: HAN, HAM, PARZN, RAMP (Fig. 5a) are obtained by multiplying the ramp function by the window functions in Fig. 4: Hann, Hamming, Parzen, Rectangular, respectively. Figure 5b gives the graphs of the convolution functions that are the inverse Fourier transform of the filter functions given in Fig. 6a. Due to assumption (ii), the filters are symmetric real valued functions. Therefore, the inverse Fourier transform of the filter $\tilde{c}_\mu$, equal to the convolution function c_μ, can be simplified:

$$c_\mu(x) = 2 \int_0^\infty \tilde{c}_\mu(f) \cos(2\pi fx)\, df \quad . \tag{31}$$

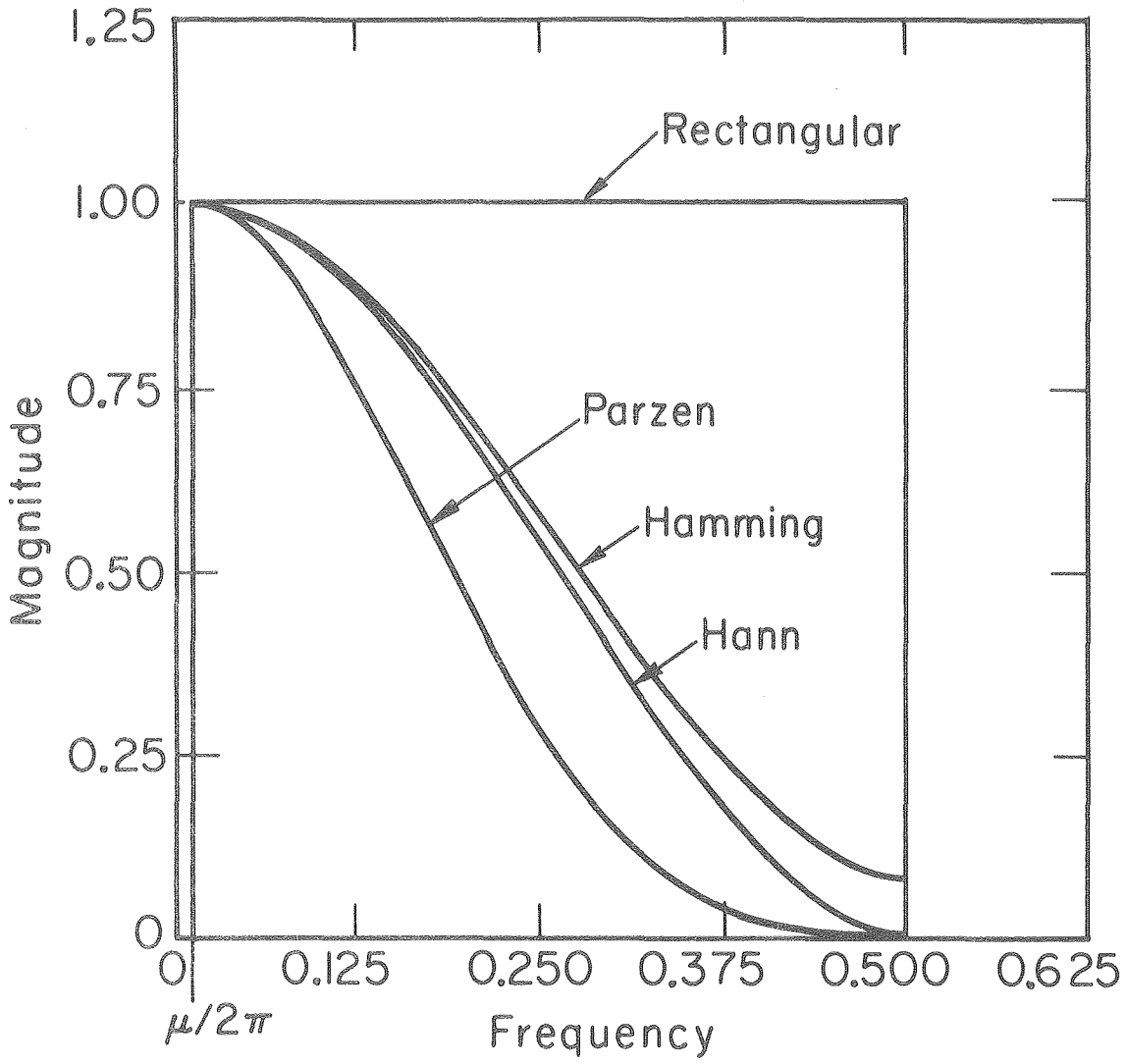

XBL803-3196

Fig. 4. These window functions are multiplied by a ramp function giving the filters shown in Fig. 5.

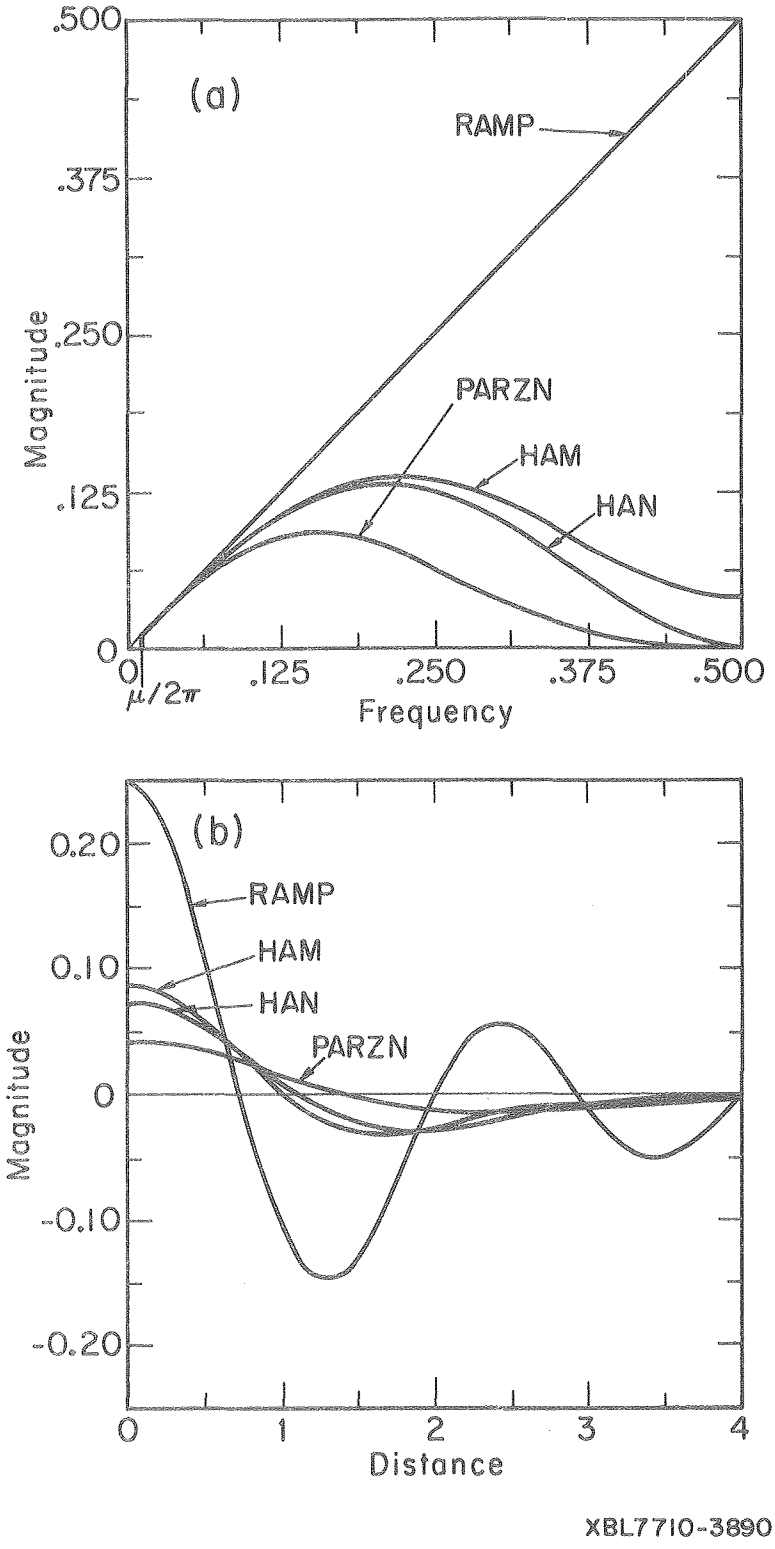

Fig. 5. (a) is the result of multiplying the window functions in Fig. 4 by a ramp function with a cut-off frequency of $f_m = 0.5$. The inverse Fourier transforms of the filters in (a) give the real space convolution functions in (b).

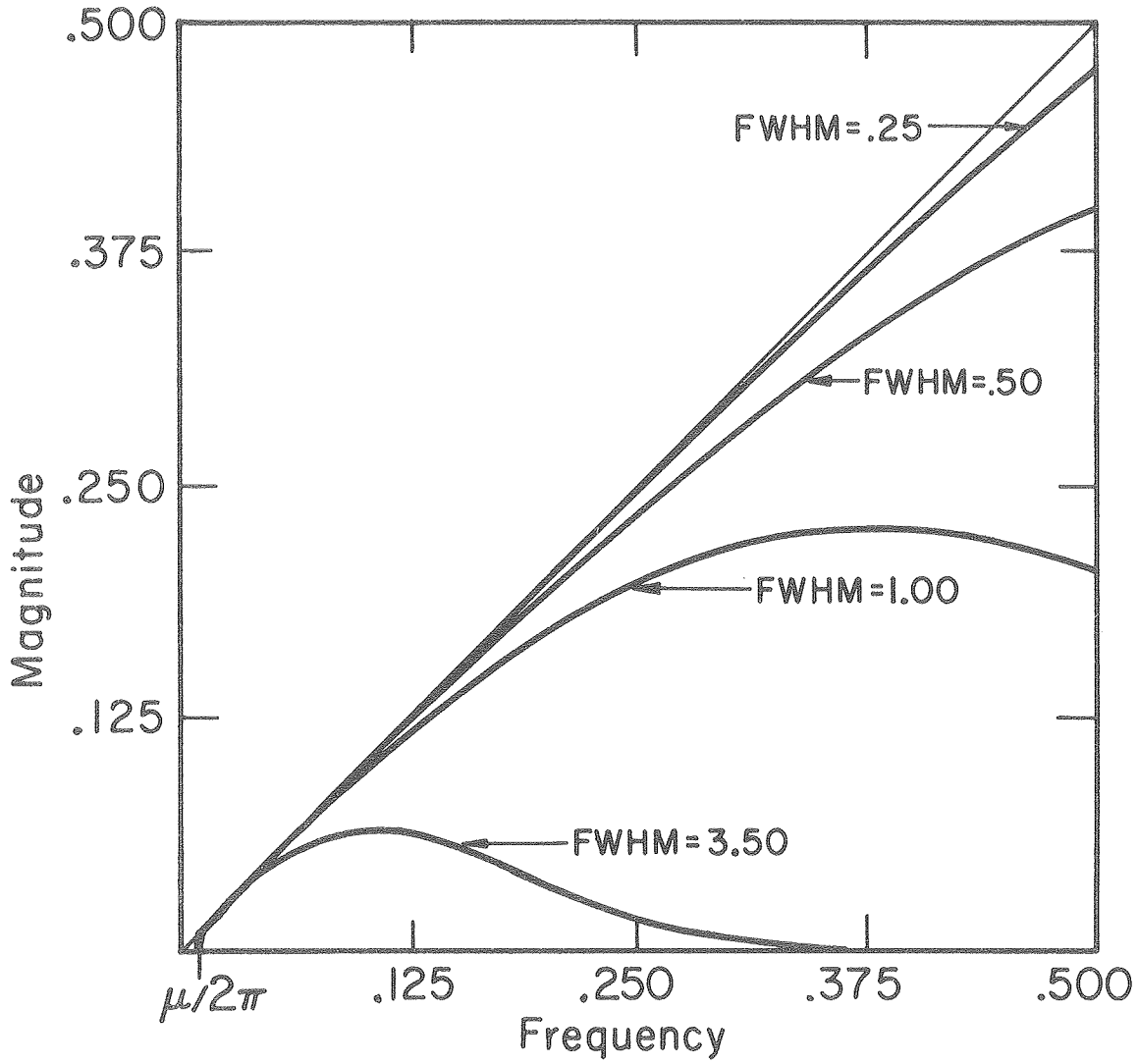

XBL802-3095

Fig. 6. The GAUSS filter for FWHM = 0.25, 0.50, 1.00, 3.50 projection bin widths; attenuation coefficient $\mu = 0.05$ (projection bin widths)$^{-1}$; and a lower cut-off frequency of $\mu/2\pi$ and an upper cut-off frequency of $f_m = 0.5$.

The distance between 0 and the first zero of the convolution function is a measure of the resolution properties of the convolver. Ideally, for good resolution, the convolution function should have a central lobe that is tall and narrow. The side lobes give rise to artifacts that are contamination from adjacent parts of the reconstruction. The side lobes amplify statistical fluctuations in the data if the lobes and data fluctuations occur at corresponding positions. Decreasing the amplitude of the side lobes will dampen the noise amplification, but such suppression will come at the cost of resolution.

Our approach uses frequency space operations. The numerical application samples the filter $\tilde{c}_\mu$ at discrete points and multiplies these by the discrete Fourier transform of sampled projections. The other approach is to sample the convolution function c_μ and convolve this with the sampled projections by assuming that the convolution function is piece-wise linear between the points $c_\mu(2kf_m)$, $k = 0,1,2,\ldots$. The two approaches give basically equivalent results for an adequate number of samples. However, due to the discrete implementation of the Fourier transform, the exact numerical results differ by a small constant [28].

The analytic expressions for the frequency filters and the corresponding real space convolution functions are shown below.

1) Rectangular Window and RAMP Filter. The rectangular window is defined by the equation

$$w_\mu(f) = \begin{cases} 1 & \text{if } \mu/2\pi \leq |f| \leq f_m \ , \\ 0 & \text{otherwise} \ , \end{cases} \tag{32}$$

where f_m is the maximum cut-off frequency.

Substituting $[s^2 + \mu^2/4\pi^2]^{\frac{1}{2}}$ for f gives

$$W_\mu(s) = \begin{cases} 1 & \text{if } 0 \leq |s| \leq [f_m^2 - \mu^2/4\pi^2]^{\frac{1}{2}} , \\ 0 & \text{otherwise} . \end{cases} \tag{33}$$

Taking the Hankel transform of $2w_\mu(s)$ gives a point spread function

$$h_\mu(r) = 2[f_m{}^2 - \mu^2/4\pi^2]^{\frac{1}{2}} \frac{J_1(2\pi[f_m{}^2 - \mu^2/4\pi^2]^{\frac{1}{2}} r)}{r} , \tag{34}$$

and for $r = 0$, $h_\mu(0) = 2\pi[f_m^2 - \mu^2/4\pi^2]$. In (34), J_1 is the first order Bessel function. The width of the central window for this point spread function becomes wider as the attenuation coefficient increases. However, for the attenuation coefficients used in nuclear medicine, $0.0958 \leq \mu \leq 0.18$ cm^{-1}, the difference in the width of the central window is insignificant. The reconstruction artifacts that arise for $\mu > 0.10$ cm^{-1} are due to the numerical methods which attempt to approximate h_μ in (34). Note also that the image cannot be restored for attenuation coefficients greater than $2\pi f_m$.

Multiplying the rectangular window by the ramp function in frequency space gives the RAMP filter

$$\tilde{c}_\mu(f) = \begin{cases} |f| & \text{if } \mu/2\pi \leq |f| \leq f_m , \\ 0 & \text{otherwise} . \end{cases}$$

The inverse Fourier transform of the RAMP filter gives the convolution function

$$c_\mu(x) = 2f_m^2\left(\frac{\sin 2\pi f_m x}{2\pi f_m x}\right) - f_m^2\left(\frac{\sin \pi f_m x}{\pi f_m x}\right)^2 - \frac{\mu^2}{2\pi^2}\left(\frac{\sin \mu x}{\mu x}\right) + \frac{\mu^2}{4\pi^2}\left(\frac{\sin \mu x/2}{\mu x/2}\right)^2 \quad . \tag{35}$$

For $\mu = 0$, $f_m = 0.5$, and $x = \ldots,-2,-1,0,1,2,\ldots$, (35) gives the convolver proposed by Ramachandran and Lakshminarayanan [5]:

$$c_o(k) = \begin{cases} \frac{1}{4} & \text{if } k = 0 \quad , \\ -\frac{1}{\pi^2 k^2} & \text{if } k \text{ odd} \quad , \\ 0 & \text{if } k \text{ even} \quad . \end{cases} \tag{36}$$

The RAMP filter (Fig. 5) gives the best resolution in the reconstructed image for perfect data but amplifies noise for data with statistical fluctuations. The sharp cut-off of the rectangular window gives a convolver with a narrow central window but side lobes which continue to oscillate even for large x. This gives rise to intensity oscillations in regions of sharp contrast and thus generates artifacts in the reconstructed image.

2) Hann Window and HAN Filter. The Hann window is defined by the equation

$$w_\mu(f) = \begin{cases} 0.5 + 0.5\cos[\pi(f^2 - \mu^2/4\pi^2)^{\frac{1}{2}}/f_m] & \text{if } \mu/2\pi \leq |f| \leq f_m \quad , \\ 0 & \text{otherwise} \quad . \end{cases} \tag{37}$$

The point spread, the HAN filter, and the convolution function are given in the following equations:

$$h_\mu(r) = 2\pi \int_0^{[f_m^2-\mu^2/4\pi^2]^{\frac{1}{2}}} 2[0.5 + 0.5\cos(\pi s/f_m)]\, J_0(2\pi rs)\, sds \qquad (38)$$

$$\tilde{c}_\mu(f) = \begin{cases} 0.5|f| + 0.5|f|\cos[\pi(f^2-\mu^2/4\pi^2)^{\frac{1}{2}}/f_m] & \text{if } \mu/2\pi \leq |f| \leq f_m \text{ ,} \\ 0 & \text{otherwise ,} \end{cases} \qquad (39)$$

$$c_\mu(x) = \int_{\mu/2\pi}^{f_m} f\left(1+\cos[\pi(f^2-\mu^2/4\pi^2)^{\frac{1}{2}}/f_m]\right)\cos(2\pi fx)\,df \quad , \qquad (40)$$

which for $\mu = 0$ reduces to

$$\begin{aligned} c_o(x) = {} & \frac{f_m^2}{2}\,\frac{\sin[f_m(2\pi x + \pi/f_m)]}{f_m(2\pi x + \pi/f_m)} - \frac{f_m^2}{4}\left(\frac{\sin[f_m(2\pi x + \pi/f_m)/2]}{f_m(2\pi x + \pi/f_m)/2}\right)^2 \\ & + f_m^2\,\frac{\sin 2\pi f_m x}{2\pi f_m x} - \frac{f_m^2}{2}\left(\frac{\sin\pi f_m x}{\pi f_m x}\right)^2 \\ & + \frac{f_m^2}{2}\,\frac{\sin[f_m(2\pi x - \pi/f_m)]}{f_m(2\pi x - \pi/f_m)} - \frac{f_m^2}{4}\left(\frac{\sin[f_m(2\pi x - \pi/f_m)/2]}{f_m(2\pi x - \pi/f_m)/2}\right)^2 . \end{aligned} \qquad (41)$$

For the Hann window the central lobe of the convolution function c_μ is wider than the central lobe of the corresponding convolution function for the rectangular window, but its side lobes are greatly reduced. Therefore, the reconstructed image has a smoother texture (less artifact) with a loss in resolution. The HAN and RAMP filters can be made to correspond closely to one another in shape and in image reconstruction results if the frequency parameter f_m of the HAN filter

is set to two times the cut-off frequency of the RAMP filter.

3) Hamming Window and HAM Filter. The Hamming window is defined by the equation

$$w_\mu(f) = \begin{cases} 0.54 + 0.46 \cos[\pi(f^2 - \mu^2/4\pi^2)^{\frac{1}{2}}/f_m] & \text{if } \mu/2\pi \leq |f| \leq f_m \ , \\ 0 & \text{otherwise} \ . \end{cases} \tag{42}$$

The point spread, the HAM filter, and the convolution function are

$$h_\mu(r) = 2\pi \int_0^{[f_m^2 - \mu^2/4\pi^2]^{\frac{1}{2}}} 2\,[0.54 + 0.46 \cos(\pi s/f_m)]\, J_0(2\pi rs)\, sds \ , \tag{43}$$

$$\tilde{c}_\mu(f) = \begin{cases} 0.54|f| + 0.46|f| \cos[\pi(f^2 - \mu^2/4\pi^2)^{\frac{1}{2}}/f_m] & \text{if } \mu/2\pi \leq |f| \leq f_m \ , \\ 0 & \text{otherwise} \ . \end{cases} \tag{44}$$

$$c_\mu(x) = \int_{\mu/2\pi}^{f_m} f(1.08 + 0.92 \cos[\pi(f^2 - \mu^2/4\pi^2)^{\frac{1}{2}}/f_m]) \cos(2\pi fx) df \ , \tag{45}$$

which for $\mu = 0$ reduces to

$$c_o(x) = 0.46\, f_m^2 \frac{\sin[f_m(2\pi x + \pi/f_m)}{f_m(2\pi x + \pi/f_m)} - 0.23\, f_m^2 \left(\frac{\sin[f_m(2\pi x + \pi/f_m)/2]}{f_m(2\pi x + \pi/f_m)/2} \right)^2$$

$$+ 1.08\, f_m^2 \frac{\sin 2\pi f_m x}{2\pi f_m x} - 0.54\, f_m^2 \left(\frac{\sin \pi f_m x}{\pi f_m x} \right)^2$$

$$+ 0.46\, f_m^2 \frac{\sin[f_m(2\pi x - \pi/f_m)]}{f_m(2\pi x - \pi/f_m)} - 0.23\, f_m^2 \left(\frac{\sin[f_m(2\pi x - \pi/f_m)/2]}{f_m(2\pi x - \pi/f_m)/2} \right)^2 . \quad (46)$$

The HAN filter has smaller extreme values in the side lobes than does the HAM filter, and the width of the central lobe is greater.

4) Parzen Window and PARZN Filter. The Parzen window is defined by the equation

$$w_\mu(f) = \begin{cases} 1 - 6 \left(\frac{[f^2 - \mu^2/4\pi^2]^{1/2}}{f_m} \right)^2 \left(1 - \frac{[f^2 - \mu^2/4\pi^2]^{1/2}}{f_m} \right) & \text{if } \mu/2\pi \leq |f| \leq f_m/2 , \\ 2 \left(1 - \frac{[f^2 - \mu^2/4\pi^2]^{1/2}}{f_m} \right)^3 & \text{if } f_m/2 < |f| \leq f_m , \\ 0 & \text{otherwise} . \end{cases} \quad (47)$$

The point spread, the PARZN filter, and the convolution function are

$$h_\mu(r) = 2\pi \sum_{m=0}^{\infty} \frac{(-1)(2\pi r)^{2m}}{2^{2m}(m!)^2} \left\{ 4 \frac{a^{2m+2}}{2m+2} - \frac{12}{f_m} \frac{a^{2m+3}}{2m+3} + \frac{12}{f_m^2} \frac{a^{2m+4}}{2m+4} \right.$$

$$\left. - \frac{4}{f_m^3} \frac{a^{2m+5}}{2m+5} - 2 \frac{b^{2m+2}}{2m+2} + \frac{12}{f_m} \frac{b^{2m+3}}{2m+3} - \frac{24}{f_m^2} \frac{b^{2m+4}}{2m+4} + \frac{16}{f_m^3} \frac{b^{2m+5}}{2m+5} \right\} , \tag{48}$$

where $a = [f_m^2 - \mu^2/4\pi^2]^{\frac{1}{2}}$ and $b = [f_m^2/4 - \mu^2/4\pi^2]^{\frac{1}{2}}$,

$$\tilde{c}_\mu(f) = \begin{cases} |f| - 6|f| \left(\frac{[f^2 - \mu^2/4\pi^2]^{\frac{1}{2}}}{f_m} \right)^2 \left(1 - \frac{[f^2 - \mu^2/4\pi^2]^{\frac{1}{2}}}{f_m} \right) \\ \qquad\qquad \text{if } \mu/2\pi \leq |f| \leq f_m/2 \ , \\ 2|f| \left(1 - \frac{[f^2 - \mu^2/4\pi^2]^{\frac{1}{2}}}{f_m} \right)^3 \qquad \text{if } f_m/2 < |f| \leq f_m \ , \\ 0 \qquad\qquad \text{otherwise} \ , \end{cases} \tag{49}$$

$$c_\mu(x) = \int_{\mu/2\pi}^{f_m} 2\, \tilde{c}_\mu(f) \cos(2\pi f x) df \ , \tag{50}$$

which for $\mu = 0$ reduces to

$$c_o(x) = [48\pi f_m x \cos 2\pi f_m x - 96 \sin 2\pi f_m x - 96\pi f_m x \cos \pi f_m x$$

$$+ 384 \sin \pi f_m x - 16\pi^3 f_m^3 x^3 - 144\pi f_m x] / (32\pi^5 f_m^3 x^5) \ , \tag{51}$$

where $c_o(0) = 0.175\, f_m^2$.

The central lobe of the Parzen window is about 30% wider than either the Hann or Hamming window, so the reconstructed image resolution is less than can be achieved with the HAN or HAM filter. On the other hand, the PARZN filter has good noise suppression.

5) Shepp and Logan Window and SHLO Filter. The Shepp and Logan window is defined by the equation

$$W_\mu(f) = \begin{cases} \dfrac{\sin[\pi(f^2 - \mu^2/4\pi^2)^{1/2}/2f_m]}{\pi(f^2 - \mu^2/4\pi^2)^{1/2}/2f_m} & \text{if } \mu/2\pi \leq |f| \leq f_m \quad , \\ 0 & \text{otherwise} \quad . \end{cases} \tag{52}$$

The point spread, the SHLO filter, and the convolution function are given in the following equations:

$$h_\mu(r) = 2\pi \int_0^{[f_m^2 - \mu^2/4\pi^2]^{1/2}} \frac{2\sin(\pi s/2f_m)}{\pi s/2f_m} J_0(2\pi rs)\, s\, ds \quad , \tag{53}$$

$$\tilde{c}_\mu(f) = \begin{cases} \dfrac{|f|\sin[\pi(f^2 - \mu^2/4\pi^2)^{1/2}/2f_m]}{\pi(f^2 - \mu^2/4\pi^2)^{1/2}/2f_m} & \text{if } \mu/2\pi \leq |f| \leq f_m \\ 0 & \text{otherwise} \quad . \end{cases} \tag{54}$$

$$c_\mu(x) = \int_{\mu/2\pi}^{f_m} \frac{f\sin[\pi(f^2 - \mu^2/4\pi^2)^{1/2}/2f_m]}{\pi(f^2 - \mu^2/4\pi^2)^{1/2}/2f_m} \cos(2\pi fx)\, df \quad , \tag{55}$$

which for $\mu = 0$ reduces to

$$c_o(x) = \frac{4f_m^2}{\pi^2}\left[\frac{1 - \sin(2\pi\, xf_m)}{1 - 4f_m x} + \frac{1 + \sin(2\pi\, xf_m)}{1 + 4f_m x}\right] . \qquad (56)$$

For $\mu = 0$, $f_m = 0.5$, and $x = \ldots,-2,-1,0,1,2,\ldots$, this gives the Shepp and Logan convolution function [6]:

$$c(k) = \begin{cases} \dfrac{2}{\pi^2} & \text{if } k = 0 \quad , \\ \dfrac{2}{\pi^2(1 - 4k^2)} & \text{if } k \neq 0 \quad . \end{cases} \qquad (57)$$

6) Gaussian Window and GAUSS Filter. The Gaussian window is defined by the equation

$$w_\mu(f) = \begin{cases} \exp[-\pi(f^2 - \mu^2/4\pi^2)\delta^2] & \text{if } \mu/2\pi \leq |f| \leq f_m \quad , \\ 0 & \text{otherwise} \quad . \end{cases} \qquad (58)$$

where f_m is the cut-off frequency and δ is a resolution parameter. The point spread function is

$$h_\mu(r) = 2\pi \sum_{n=0}^{\infty}\sum_{m=0}^{\infty} (-1)^{n+m} \frac{\delta^{2n}\, \pi^{2m+n}[f_m^2 - \mu^2/4\pi^2]^{n+m+1}}{n!\ (m!)^2\ (n+m+1)}\, r^{2m} \qquad (59)$$

where $h_\mu(0) = \frac{2}{\delta^2}[1 - \exp(-\pi\delta^2[f_m^2 - \mu^2/4\pi^2])]$. For $f_m = \infty$ this reduces to the Gaussian distribution

$$h_\mu(r) = \frac{2}{\delta^2} e^{-\pi r^2/\delta^2} \quad . \tag{60}$$

The full-width at half maximum (FWHM) of the point spread function in (60) is related to the parameter δ by the equation

$$\delta^2 = \frac{\pi(\text{FWHM})^2}{4\ell n(2)} \quad . \tag{61}$$

In Section VII, we will use FWHM as the resolution parameter even though the full-width at half maximum of $h_\mu(r)$ equals FWHM only if we sample infinitely fine. The GAUSS filter and convolution functions are

$$\tilde{c}_\mu(f) = \begin{cases} |f| \exp[-\pi(f^2 - \mu^2/4\pi^2)\delta^2] & \text{if } \mu/2\pi \leq |f| \leq f_m \quad , \\ 0 & \text{otherwise} \quad , \end{cases} \tag{62}$$

$$c_\mu(x) = \int_{\mu/2\pi}^{f_m} 2f \exp[-\pi(f^2 - \mu^2/4\pi^2)\delta^2] \cos(2\pi f x)\, df \quad . \tag{63}$$

As FWHM increases, the GAUSS filter is shown in Fig. 6 to deviate more and more from a ramp filter. Increasing FWHM causes the resolution to deteriorate. However, increasing FWHM suppresses statistical fluctuations.

7) Butterworth Window and BUTER Filter. The major advantage of the BUTER filter is that it can be modified according to the amount of noise in the projection data. The filter is derived by using the square of the magnitude of the Butterworth filter as a window function

$$w_\mu(f) = \frac{1}{1 + [(f^2 - \mu^2/4\pi^2)^{\frac{1}{2}}/f_m]^{2n}} \tag{64}$$

where f_m is a frequency parameter and n is the order of the filter. This is multiplied by the ramp function giving the BUTER filter

$$\tilde{c}_\mu(f) = \frac{|f|}{1 + [(f^2 - \mu^2/4\pi^2)^{\frac{1}{2}}/f_m]^{2n}} \quad . \tag{65}$$

The shape of the filter is determined by f_m and n where n can be any real value. A value for n may be in the range of 5 to 350 and a value for f_m between 0.25 and 1.

The filter is designed by calculating the appropriate window widths between 0 and f_p and the corresponding transition bands between the pass-band frequency f_p and the stop-band frequency f_s as illustrated in Fig. 7. If the values of ε, A, f_p and f_s are known for a particular window, then the parameters n and f_m of the Butterworth filter are determined using the equations [32]

$$n = \frac{\log[\varepsilon/(A^2 - 1)^{\frac{1}{2}}]}{\log[(f_p^2 - \mu^2/4\pi^2)^{\frac{1}{2}}/(f_s^2 - \mu^2/4\pi^2)^{\frac{1}{2}}]} \quad , \tag{66}$$

$$f_m = \frac{(f_p^2 - \mu^2/4\pi^2)^{\frac{1}{2}}}{\varepsilon^{1/n}} \quad . \tag{67}$$

The window defined by (64) can be designed so that it has either a narrow transition band between f_p and f_s, thus approaching a rectangular window, or a wide transition band such as the Hann or Hamming window. A window function with a narrow transition band in frequency space is equivalent to having a narrow central lobe for the point spread function, which means that the reconstruction will have good resolution with high statistics, but concurrently the side lobes for such a window function are larger, thus amplifying noise for low statistics. On the other hand, a wider transition band gives poorer spatial resolution with reduced noise amplification.

8) Wiener Window and MMSE Filter. Thus far we have discussed filters varying in noise suppression, resolution, and attenuation coefficient. The shape of the filter also depends on the object to be reconstructed. A more flexible filter than those presented thus far has a frequency response that can accommodate both the frequency spectrum of the object to be reconstructed and its noise level. Such a filter, minimizing the error between the true image and an optimum linear estimate of the true image, was derived for $\mu = 0$, based on the solution of the Wiener-Hopf equation [29],[30]. The modification of this filter for $\mu > 0$ is

$$\tilde{c}_\mu(f) = \frac{|f|}{1 + \gamma \dfrac{(f^2 - \mu^2/4\pi^2)^{\frac{1}{2}}\,\bar{m}}{S([f^2 - \mu^2/4\pi^2]^{\frac{1}{2}})}} \quad , \tag{68}$$

where $\bar{m}$ is the mean of the projection data, S is the power spectrum of the projection data (estimated by the square of the Fourier transform), and γ is a weighting factor on the noise-to-signal term of (68). This is the MMSE filter which is equal to the Wiener window multiplied by the ramp function $|f|$.

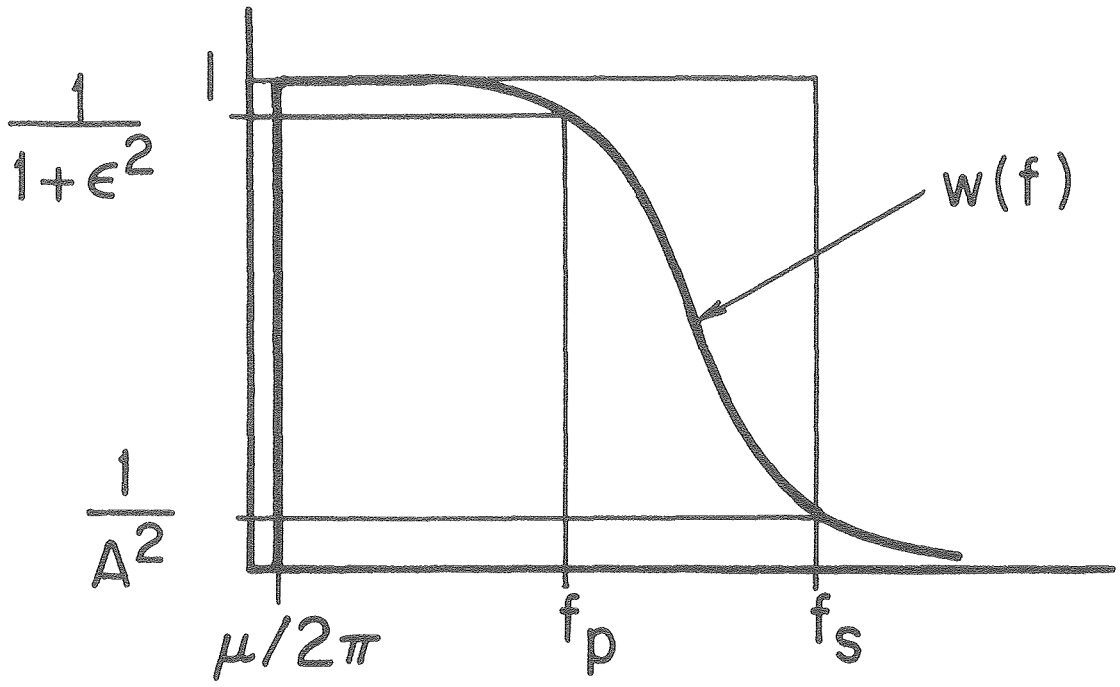

XBL803-3195

Fig. 7. Method of designating a Butterworth filter. The parameters ε and A are calculated from ordinates at the selected pass frequency f_p and stop frequency f_s. The window function has a lower cut-off frequency of $\mu/2\pi$.

VI. STATISTICAL FORMULAS FOR FILTERING METHODS

For variable attenuation, errors in the reconstructed image are the result of statistical fluctuations in both transmission and emission data [2]. For constant attenuation, the noise propagated by the convolution algorithm is the result of statistical fluctuations only in the emission data. If these fluctuations are statistically independent and Poisson distributed, the estimate of the variance and mean for the random variable of each projection is the measured projection value:

$$E\{p(\xi,\theta)\} = \sigma^2\{p(\xi,\theta)\} = p(\xi,\theta) \quad . \tag{69}$$

Therefore, the estimates for the mean and variance of the modified projections in (15) are

$$E\{p(\xi,\theta)\} = p(\xi,\theta)\, e^{\mu\beta(\xi,\theta)} \tag{70}$$

$$\sigma^2\{p(\xi,\theta)\} = p(\xi,\theta)\, e^{2\mu\beta(\xi,\theta)} \quad . \tag{71}$$

Making the assumption that our data samples represent independent Poisson random variables, we will give expressions for the mean value, variance, percent root-mean-square (%RMS) uncertainty, and covariance functions using (70) and (71).

Using the formula

$$m_\rho(\underset{\sim}{r}) = \mathcal{B}_\mu \{ c_\mu(\xi) * E[p(\xi,\theta)] \} \quad , \tag{72}$$

the mean value function $m_\rho(\underset{\sim}{r})$ for the reconstruction, expressed in terms of the measured projections, is

$$m_\rho(\underset{\sim}{r}) = \mathcal{B}_\mu\left\{c_\mu(\xi) * p(\xi,\theta)\, e^{\mu\beta(\xi,\theta)}\right\} \quad . \tag{73}$$

The variance function for the reconstructed image is by definition

$$\sigma^2_\rho(\underset{\sim}{r}) = E\left\{[\rho(\underset{\sim}{r}) - E[\rho(\underset{\sim}{r})]]^2\right\} \quad . \tag{74}$$

For independent projection samples, this reduces to [34]

$$\sigma^2_\rho(\underset{\sim}{r}) = \mathcal{B}_{2\mu}\left\{c^2_\mu(\xi) * \sigma^2[p(\xi,\theta)]\right\} \quad . \tag{75}$$

Thus, in terms of the projection data, the variance function is

$$\sigma^2_\rho(\underset{\sim}{r}) = \mathcal{B}_{2\mu}\left\{c_\mu(\xi)^2 * [p(\xi,\theta)\, e^{2\mu\beta(\xi,\theta)}]\right\} \quad . \tag{76}$$

With the results in (73) and (76), the %RMS uncertainty in the reconstructed image is

$$\%\text{RMS uncertainty}(r) = \frac{100\left\{\sigma^2_\rho(\underset{\sim}{r})\right\}^{\frac{1}{2}}}{m_\rho(\underset{\sim}{r})} \tag{77}$$

$$= \frac{100[\mathcal{B}_{2\mu}\left\{c_\mu(\xi)^2 * [p(\xi,\theta)\, e^{2\mu\beta(\xi,\theta)}]\right\}]^{\frac{1}{2}}}{\mathcal{B}_\mu\left\{c_\mu(\xi) * [p(\xi,\theta)\, e^{\mu\beta(\xi,\theta)}]\right\}} \tag{78}$$

Note that the %RMS uncertainty is a function of position in the transverse section.

The autocovariance function,

$$C_{\rho\rho}(\underset{\sim}{r}_1,\underset{\sim}{r}_2) = E\left\{[\rho(\underset{\sim}{r}_1) - m_\rho(\underset{\sim}{r}_1)]\,[\rho(\underset{\sim}{r}_2) - m_\rho(\underset{\sim}{r}_2)]\right\} \quad , \tag{79}$$

gives a measure of the "texture" of the reconstructed noise. For single-photon ECT with constant attenuation this reduces to

$$C_{\rho\rho}(\underset{\sim}{r}_1,\underset{\sim}{r}_2) = \int_0^{2\pi}\int_{-\infty}^{\infty} c_\mu(\langle \underset{\sim}{r}_1,\underset{\sim}{\theta}\rangle - \xi)\, e^{-\mu\langle \underset{\sim}{r}_1,\underset{\sim}{\theta}^\perp\rangle} \times c_\mu(\langle \underset{\sim}{r}_2,\underset{\sim}{\theta}\rangle - \xi)\, e^{-\mu\langle \underset{\sim}{r}_2,\underset{\sim}{\theta}^\perp\rangle}\, \sigma^2\{p(\xi,\theta)\}d\xi d\theta \quad . \tag{80}$$

When $\underset{\sim}{r}_1 = \underset{\sim}{r}_2$ in (80), the autocovariance is equal to the variance given by (75). Below, we examine the noise properties and covariance functions for a simple point source distribution and a distributed circular disc source.

1) Point Source Image. For a point source image $\rho(x,y) = \delta(x - x_o)(y - y_o)$, the measured projection, the mean, the variance, and the covariance functions follow from (15), (73), (76), (80):

$$p(\xi,\theta) = e^{-\mu\beta(\xi,\theta)}\, e^{\mu\langle \underset{\sim}{r}_o,\underset{\sim}{\theta}^\perp\rangle}\, \delta(\xi - \langle \underset{\sim}{r}_o,\underset{\sim}{\theta}\rangle) \quad , \tag{81}$$

$$m_\rho(\underset{\sim}{r}) = \int_0^{2\pi} c_\mu[\langle \underset{\sim}{r} - \underset{\sim}{r}_o,\underset{\sim}{\theta}\rangle]\, e^{-\mu\langle \underset{\sim}{r}-\underset{\sim}{r}_o,\underset{\sim}{\theta}^\perp\rangle}\, d\theta \quad , \tag{82}$$

$$\sigma_\rho^2(\underset{\sim}{r}) = \int_0^{2\pi} c_\mu^2[\langle \underset{\sim}{r} - \underset{\sim}{r}_o,\underset{\sim}{\theta}\rangle]\, e^{\mu\beta(\langle \underset{\sim}{r}_o,\underset{\sim}{\theta}\rangle,\theta)}\, e^{-2\mu\langle \underset{\sim}{r}-\underset{\sim}{r}_o,\underset{\sim}{\theta}^\perp\rangle}\, d\theta \quad , \tag{83}$$

$$C_{\rho\rho}(\underset{\sim}{r}_1,\underset{\sim}{r}_2) = \int_0^{2\pi} c_\mu[\langle \underset{\sim}{r}_1-\underset{\sim}{r}_o,\underset{\sim}{\theta}\rangle]\, c_\mu[\langle \underset{\sim}{r}_2-\underset{\sim}{r}_o,\underset{\sim}{\theta}\rangle]\, e^{\mu\beta(\langle \underset{\sim}{r}_o,\underset{\sim}{\theta}\rangle,\theta)} \times e^{-\mu\langle \underset{\sim}{r}_1+\underset{\sim}{r}_2-\underset{\sim}{r}_o,\underset{\sim}{\theta}^\perp\rangle}\, d\theta \quad . \tag{84}$$

If $\underset{\sim}{r}_0 = 0$, the mean value function $m_\rho(\underset{\sim}{r})$ is just the point spread function h_μ given by (23) and the variance is the back-projection $\mathcal{B}_{2\mu}$ of the square of the convolution function multiplied by the exponential factor $e^{\mu\beta(0,\theta)}$. Thus, the average value in (82) is very local, whereas the variance (83) has a much larger extent.

2) Circular Disc. For a distributed source in a circular disc of radius R and attenuation coefficient μ, the measured projection, the mean, and the variance functions are

$$p(\xi,\theta) = \begin{cases} e^{-\mu(R^2-\xi^2)^{\frac{1}{2}}} \dfrac{2}{\pi R^2} \dfrac{C}{\mu} \sinh[\mu(R^2-\xi^2)^{\frac{1}{2}}] & , \quad |\xi| \leq R \\ 0 & , \quad \text{otherwise} \end{cases} \tag{85}$$

$$m_\rho(\underset{\sim}{r}) = \frac{2C}{\pi R^2 \mu} \mathcal{B}_\mu\{c_\mu(\xi) * \sinh[\mu(R^2-\xi^2)^{\frac{1}{2}}]\} \tag{86}$$

$$\sigma^2_\rho(\underset{\sim}{r}) = \frac{2C}{\pi R^2 \mu} \mathcal{B}_{2\mu}\left(c^2_\mu(\xi) * \{\sinh[\mu(R^2-\xi^2)^{\frac{1}{2}}] \exp[\mu(R^2-\xi^2)^{\frac{1}{2}}]\}\right) \tag{87}$$

where C is the total emitted photons over the disc.

For a circular disc the %RMS uncertainty defined by (77) is given by

$$\%\text{RMS uncertainty} = \left(\frac{A}{C}\right)^{\frac{1}{2}} \tag{88}$$

where A represents the factors not including C after dividing (87) by the square of (86) and multiplying by 10^4. The square of the %RMS uncertainty is inversely proportional to the total emitted photons. Since the emitted and the measured photons are related by a constant

attenuation factor independent of C, (88) is also valid if we interpret C to be total measured photons.

VII. RESULTS

Reconstructions of simulated data were performed using the BKFIL algorithm expressed in (18) and illustrated in Fig. 8. The algorithm used the GAUSS filter function (see (62) and Fig. 6). For small values of FWHM, the GAUSS filter corresponds to the ramp filter. Large values of the FWHM for the GAUSS filter correspond to a roll-off implemented by the HAN, HAM and PARZN filters. Remember that the full-width-at-half-maximum of the point spread function for the GAUSS filter approximately equals FWHM. The full-width-at-half-maximum can equal FWHM only if projection samples are continuous both laterally and in angle.

The hot spot phantom in Fig. 9 was used to simulate the resolution capabilities of the filters. The phantom is 20 cm in diameter, represented by a 128 x 128 pixel array with 1.56 mm per pixel. The phantom was reconstructed from 180 projection angles over 360°. The projections had bin sizes equal to the pixel size and were evaluated using analytically calculated line integrals.

The data, which conformed to the projections given by (15), were reconstructed for $\mu = 0.15\ cm^{-1}$ and $\mu = 0.25\ cm^{-1}$ using the GAUSS filter parameters FWHM = 0.25, 1.00, 3.50, and 6.00 projection bin widths (pbw) (0.04, 0.16, 0.55, 0.94 cm). For $\mu = 0.15\ cm^{-1}$ the resolution of the reconstructions deteriorates as FWHM increases. For $\mu = 0.25\ cm^{-1}$ the results are somewhat opposite than that of $\mu = 0.15\ cm^{-1}$. The resolution

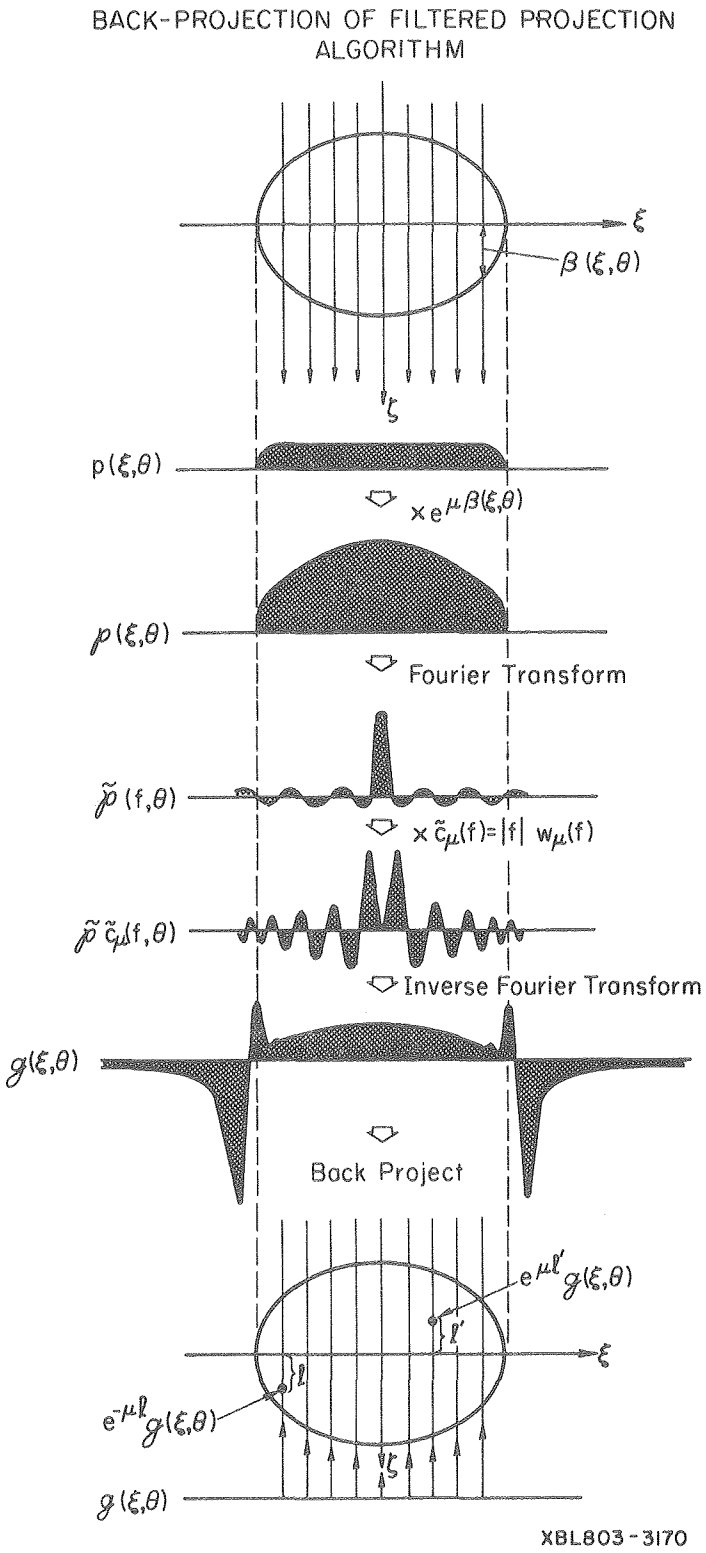

Fig. 8. Back-projection of filtered projection algorithm (BKFIL).

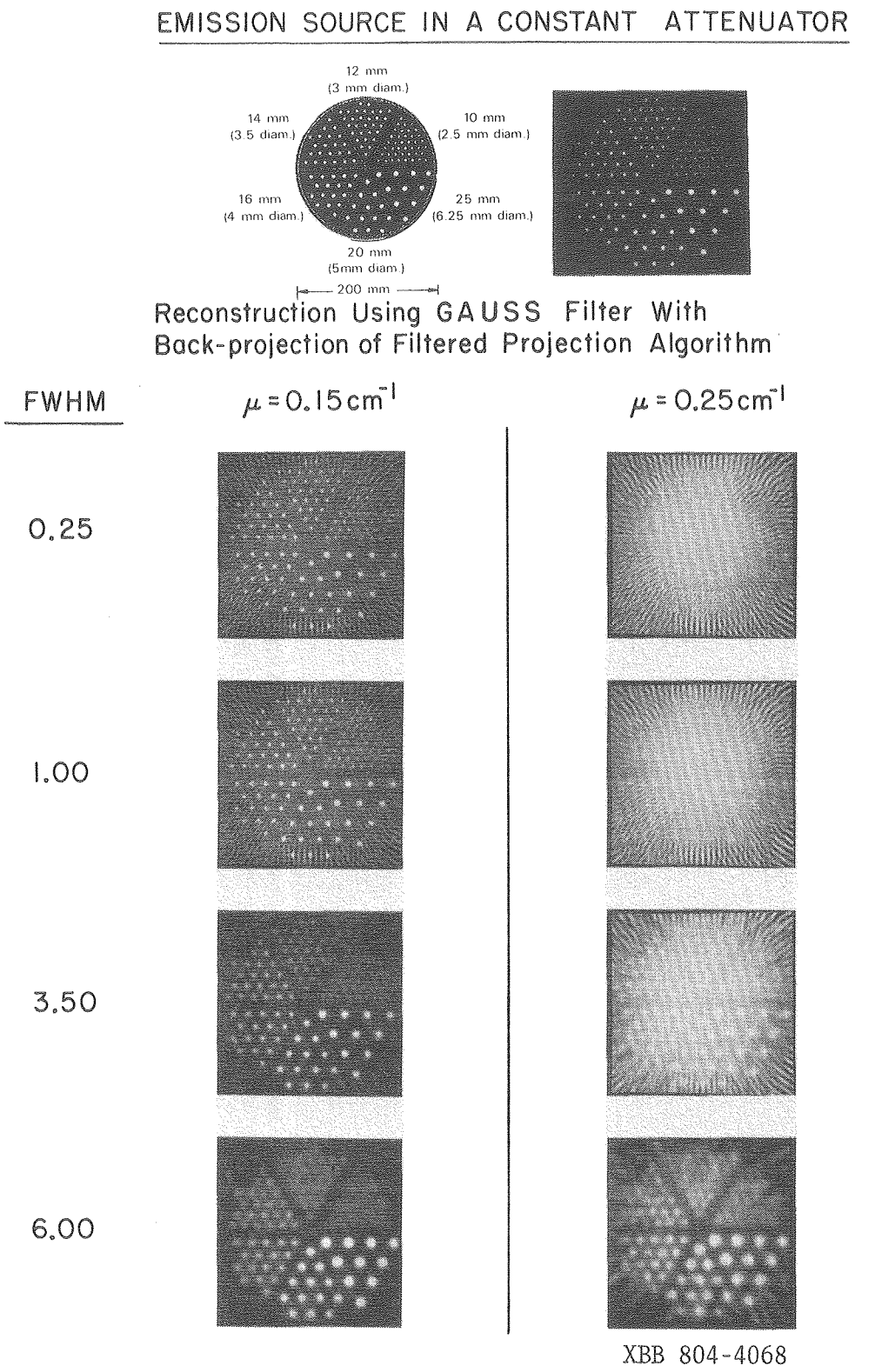

Fig. 9. Reconstructions of a 20-cm hot spot phantom. The pixel and projection bin sizes are 1.56 mm. The phantom was reconstructed by applying a GAUSS filter with FWHM = 0.25, 1.00, 3.50 and 6.00 projection bin widths to 180 projections equally sampled over 360°.

improved as FWHM went from 0.25 to 3.50 pbw, but again showed a blurred image for FWHM = 6.00 pbw.

Simulations were performed whereby the hot spot phantom was blurred by the point spread function for the ramp filter given in (34). The point spread function did not blur the image except for high attenuation coefficients ($\mu \approx \pi$ pixel^{-1}). Thus, these simulations did not correlate with the reconstruction results in Fig. 9 for μ = 0.25 cm^{-1} and FWHM = 0.25 pbw. To investigate this discrepancy, the hot spot phantom was reconstructed with 360 and 720 projection angles. The results in Fig. 10 show considerable improvement with increase in the number of angles. For the higher attenuation coefficient of μ = 0.25 cm^{-1}, the results in Figs. 9 and 10 suggest that a ramp-type filter amplifies aliasing artifacts caused by insufficient angular sampling, but by rolling off the filter or increasing angular sampling, this amplification is reduced. Such aliasing artifacts in TCT have previously been analyzed by Crawford and Kak [35].

The application of these filters to biological problems such as reconstructing ^{99m}Tc distributed in the head were simulated using the Shepp and Logan head phantom [6]. The phantom is represented by a 64 x 64 array with 0.33 cm per pixel. The 360 projections over 360° were evaluated using analytically calculated line integrals with an attenuation distribution as shown in Fig. 11. The projection data were then modified as shown in step 2 of Fig. 8 using (15) and assuming a constant attenuation coefficient of 0.149 cm^{-1}. These modified projections were reconstructed using the GAUSS filter with FWHM = 0.25, 0.50, 1.00, 2.00, 3.00 and 3.50 projection bins widths corresponding to 0.08, 0.16, 0.33, 0.66, 1.00, and 1.16 cm, respectively. The results show the expected blurring as the

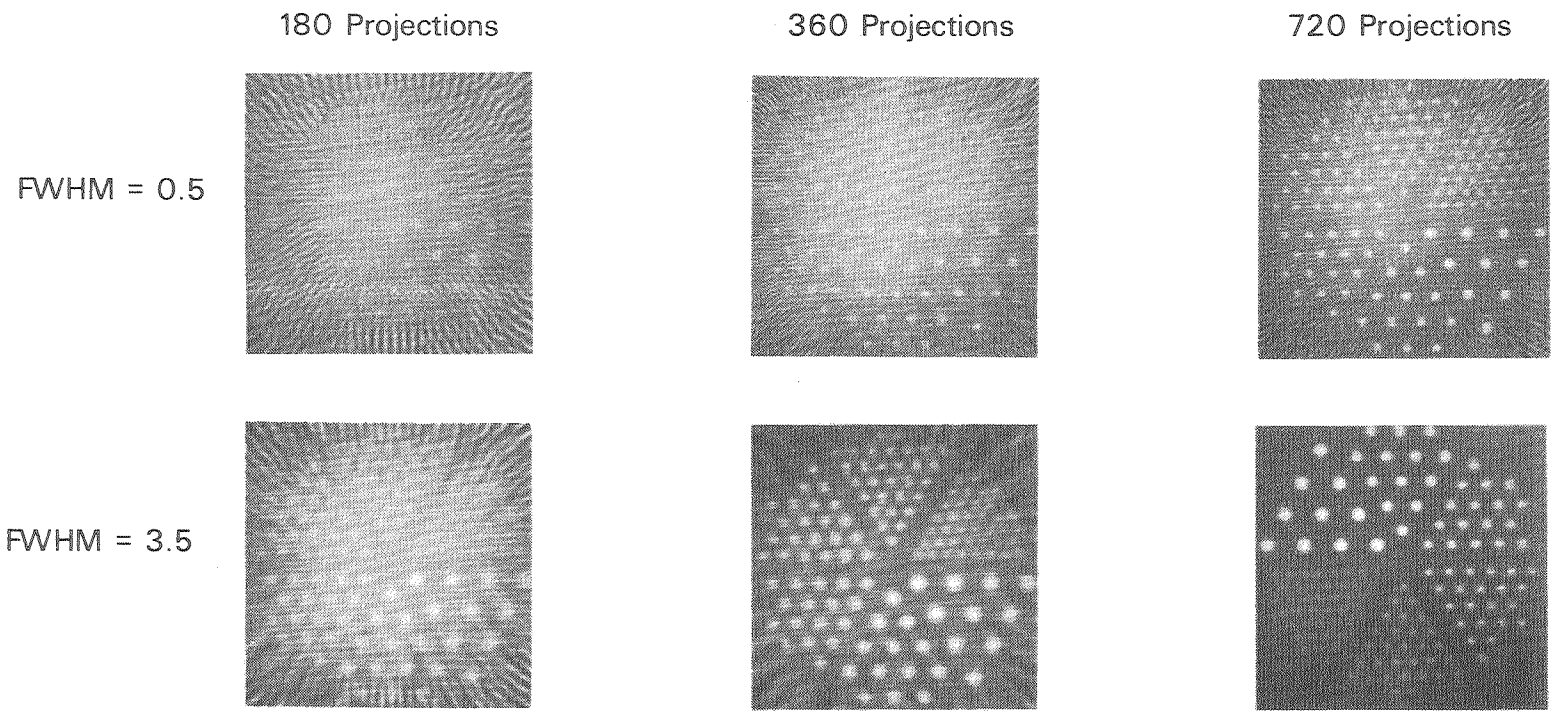

Fig. 10. Reconstruction as a function of angular sampling using the GAUSS filter. The simulated projection data were evaluated from line integrals using an attenuation coefficient of $\mu = 0.25\ cm^{-1}$ for 180, 360, and 720 projections equally sampled over 360°.

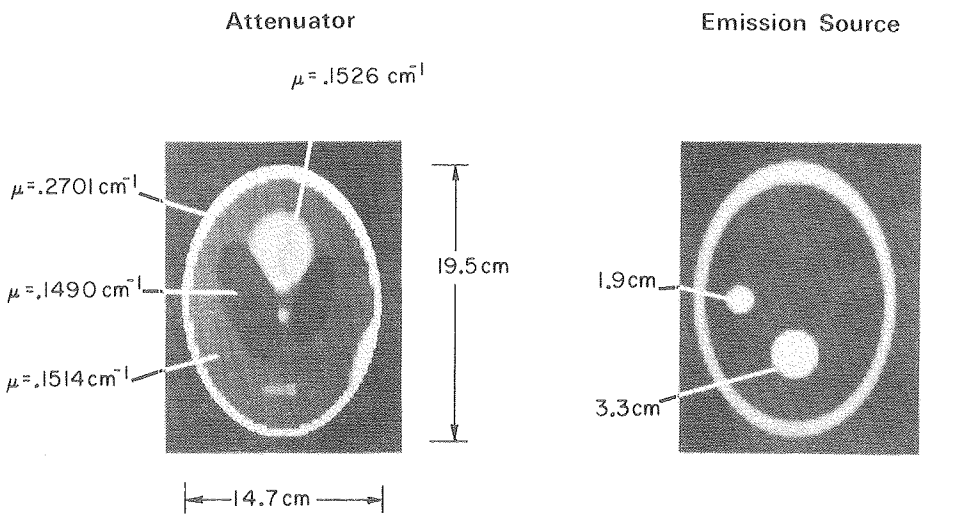

Reconstruction Using GAUSS Filter With
Back-Projection of Filtered Projection Algorithm

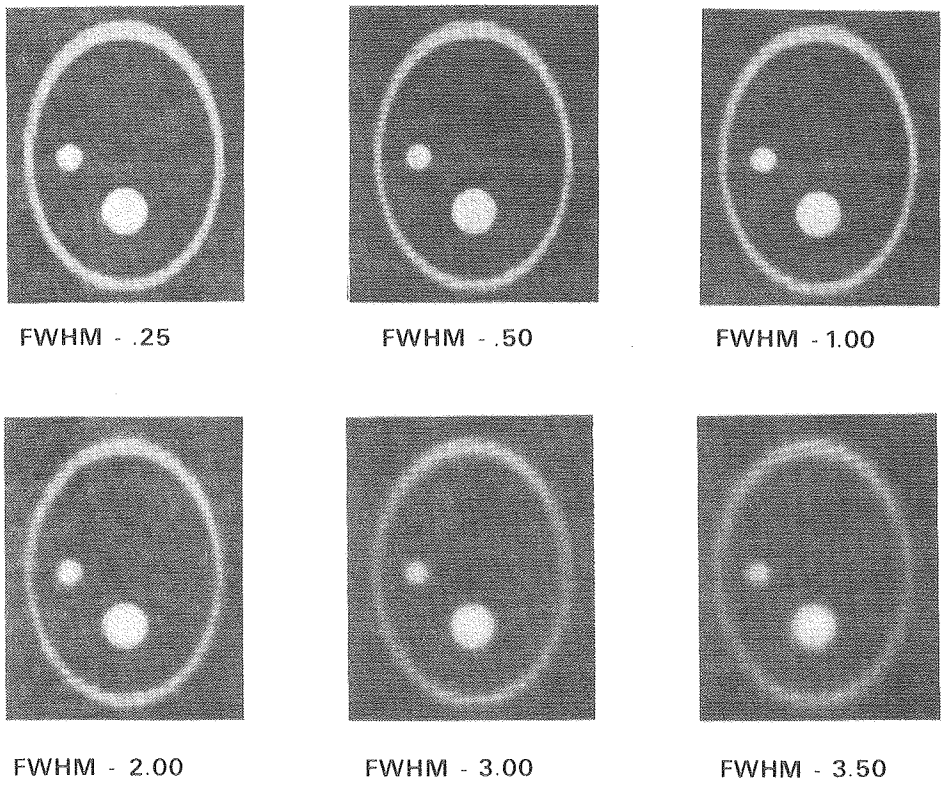

XBB 804-5034

Fig. 11. Head simulation. The simulated projection data were attenuated using the Shepp and Logan head phantom shown in the upper left figure. The 360 projections of 1° increments were reconstructed assuming a constant attenuation coefficient of $\mu = 0.149\ cm^{-1}$.

point response function becomes wider (i.e., increase in high frequency cut-off). Note that no serious artifacts arose despite the variation in attenuation of bone, gray matter, and white matter.

A circular disc of 20 cm in diameter with a resolution of 0.33 cm per pixel was chosen to simulate the propagation of errors for the BKFIL algorithm (Fig. 12). The disc was reconstructed from 360 projection angles over 360°. The projections had bin sizes equal to the pixel size of 0.33 cm. The projection data were evaluated using analytically calculated line integrals with Poisson noise whose mean and variance were equal to the measured line integral. The projection data were then modified as given by (15) and the reconstruction followed the scheme used above and depicted in Fig. 8.

These data were reconstructed for various statistics using the GAUSS filter for FWHM = 0.5, 2.00, 3.5 pbw and μ = 0.075, 0.0958, 0.149 0.18, 0.25 cm^{-1}. The results for FWHM = 0.50, 3.50 pbw and μ = 0.0958, 0.149, 0.18 cm^{-1} are shown in Fig. 12. As expected, the filters with FWHM = 0.05 pbw amplify the noise at low statistics and high attenuation coefficient, resulting in reconstruction artifacts. By rolling off the ramp (i.e., FWHM = 3.5 pbw) this amplification is reduced.

The %RMS uncertainties for the reconstructions in Fig. 12 are tabulated in Table 1 using the equations

$$\bar{\rho} = \sum_{i,j \in \Lambda} \frac{\rho_{ij}}{N} \tag{89}$$

$$\sigma^2(\rho) = \sum_{i,j \in \Lambda} \frac{(\rho_{ij} - \bar{\rho})^2}{N-1} \tag{90}$$

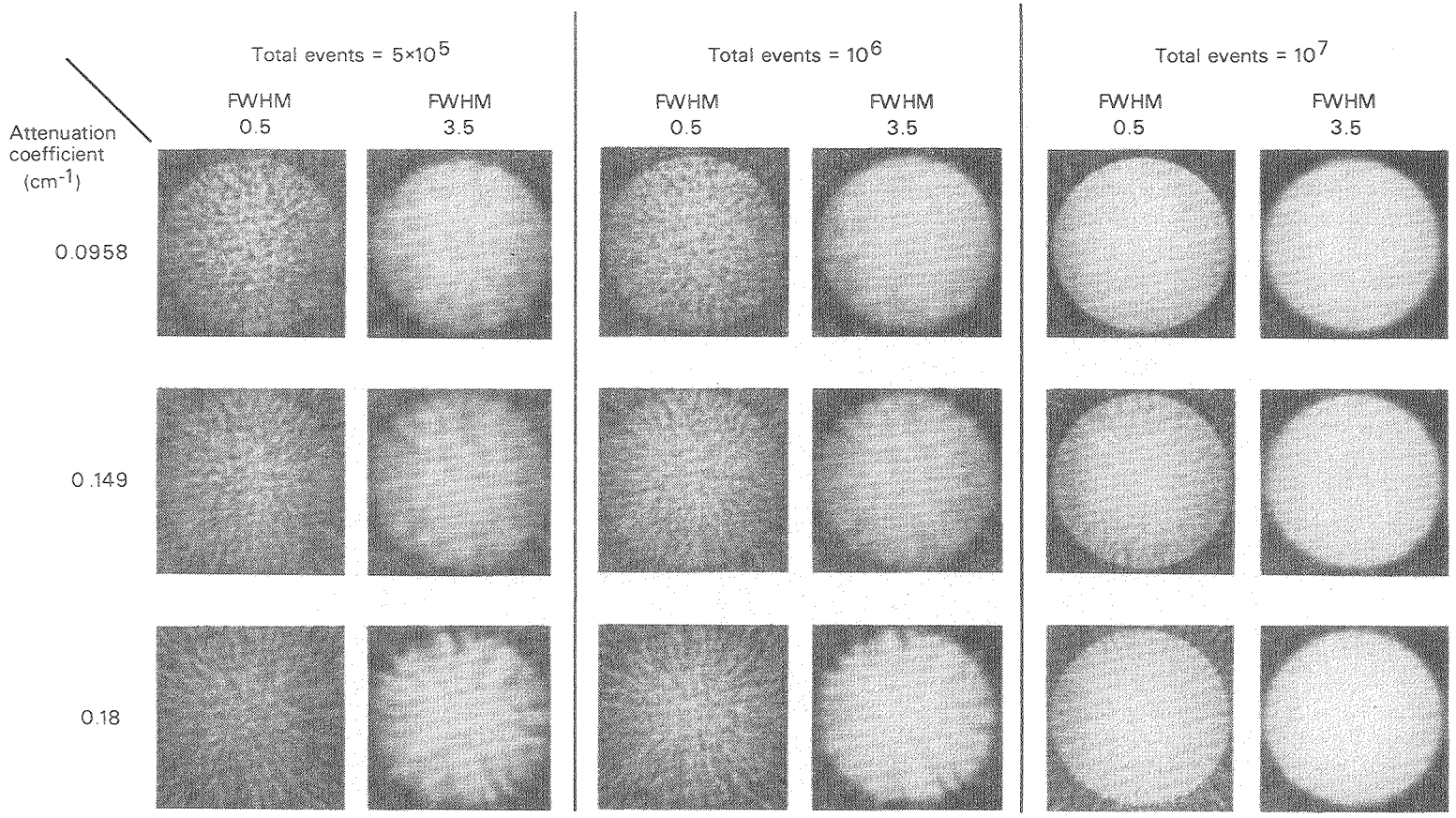

XBB 803-3566

Fig. 12. Reconstructions of a 20-cm diameter disc using a GAUSS filter with FWHM = 0.5 and 3.5 projection bin widths applied to 360 equally spaced projections bewtween 0 and 2π. The simulated projections were Poisson distributed data attenuated by constant attenuation coefficients of 0.0958, 0.149, and 0.18 cm^{-1}. The pixel and projection bins are 0.33 cm.

$$\%\text{RMS uncertainty} = \frac{100\,\sigma(\rho)}{\bar{\rho}} \tag{91}$$

where N is the number of pixels sampled for the region of interest Λ with reconstruction values ρ_{ij}. It is assumed here that the sample average over the disc closely approximates the spatial average. The results indicate that the %RMS uncertainty 1) decreases with an increase in the total measured photons for each attenuation coefficient; 2) increases with an increase in the attenuation coefficient for the same measured photons; and 3) decreases with an increase in FWHM for the same measured photons and the same attenuation coefficient. These simulations show that the contrast resolution is a function of attenuation coefficient, statistics, and filter shape.

The values for the constant A in Table 1 were obtained for each attenuation coefficient μ and filter parameter FWHM by fitting the tabulated data to (88). The variation in A for different attenuation coefficient distributions and filter shapes changes the plot of %RMS uncertainty vs. total measured counts shown in Fig. 13. It is not obvious what the functional relationship is between the %RMS uncertainty and the parameters μ and FWHM since the mean value function in (86) and the variance function in (87) depend in a more complicated way on μ and FWHM than on C (the total measured counts).

TABLE 1. %RMS uncertainties = $(A/counts)^{\frac{1}{2}}$ for the reconstructions in Fig. 12.

Attenuation coefficient (cm^{-1})	Counts					
	5×10^5	1×10^6	5×10^6	1×10^7	∞	$A/10^8$
			FWHM = 0.50			
0.075	44.0	31.3	13.7	9.94	0.77	9.71
0.0958	46.3	32.2	14.4	10.2	0.50	10.58
0.149	92.6	65.6	26.9	20.1	1.47	42.45
0.18	97.2	66.6	30.3	21.3	0.38	46.23
0.25	244.	167.	73.6	52.3	0.48	289.63
			FWHM = 2.00			
0.075	16.2	11.9	5.13	3.68	0.85	1.35
0.0958	16.7	8.30	5.51	3.87	0.58	1.19
0.149	33.9	23.2	9.94	7.60	1.56	5.60
0.18	37.6	22.7	10.9	8.03	0.44	6.40
0.25	90.1	59.6	27.3	19.2	0.53	38.74
			FWHM = 3.50			
0.075	7.87	5.64	2.80	2.29	1.59	0.331
0.0958	7.88	6.16	3.03	2.39	1.52	0.335
0.149	15.6	11.3	5.03	4.11	1.79	1.26
0.18	18.0	10.7	5.39	4.16	1.58	1.48
0.25	44.4	28.6	13.5	8.85	1.76	9.25

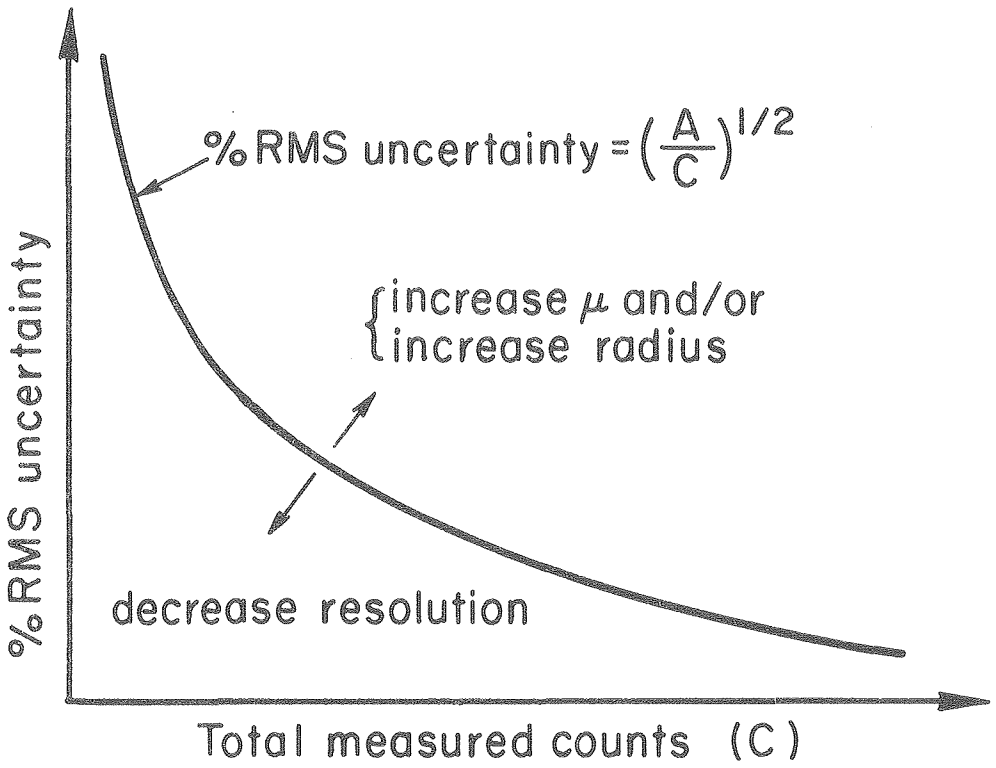

XBL803-3194

Fig. 13. Plot of %RMS uncertainty versus total measured counts. If the constant attenuation coefficient μ and/or the radius of the attenuator increases, then the curve will shift upward, whereas if the resolution decreases the curve will shift downward.

VIII. CONCLUSION

We have shown from computer simulations that filtering methods used in TCT and positron ECT apply also to single-photon ECT in the presence of a constant attenuation coefficient. In the case of TCT and positron ECT the filtering approach is derived directly from the Fourier projection theorem. For single-photon ECT, however, the Fourier projection theorem [16] does not permit a straightforward filtering approach without first interpolating the Fourier transform of each projection [14],[15]. In the case of single-photon ECT a space-invariant point spread function can be obtained using the BKFIL algorithm by a simple modification of the filter and back-projection operator.

The filters are zero for frequencies less than $\mu/2\pi$ and greater than f_m cycles per projection bin. For the ramp filter the point spread function for continuous sampling is

$$h_\mu(r) = 2z \frac{J_1(2\pi\, zr)}{r} \tag{92}$$

where $z = [f_m^2 - \mu^2/4\pi^2]^{\frac{1}{2}}$. This point spread function gives insight into the response of the BKFIL algorithm for different attenuation coefficients. For the factor z to be greater than zero, f_m must be greater than $\mu/2\pi$. Therefore, if f_m is set so that the sampling criterion is met — i.e., the sampling interval is $1/(2f_m)$ — then the image cannot be reconstructed if the projections have been attenuated by a coefficient greater than $2\pi f_m$ ($\mu < 2\pi f_m$). Put another way, if the attenuation coefficient is $\mu = 0.15\ cm^{-1}$, then the sampling interval must be at least 20.9 cm. This seems to be a somewhat trivial requirement since all

scintillation cameras have a resolution much finer than this. However, it does reveal the interplay between the attenuation coefficient and sampling requirements. An implication of (92) is the requirement that the sampling interval must decrease as μ increases for a constant point spread function; i.e., to have the same point spread function as at $\mu = 0$, f_m must increase as given by $f_m(\mu) = [f_m(0) + \mu^2/4\pi^2]^{\frac{1}{2}}$ so that z remains constant. Recall that in the numerical implementation, $f_m = 0.5$ cycles per projection bin. Therefore, if the sampling interval is decreased, the value of μ in units of cycles per projection bin decreases.

The point spread function for the ramp filter in (92) indicates that significant blurring should not occur for isotopes used in nuclear medicine with attenuation coefficients between zero and 0.18 cm^{-1}. Simulations have shown that for continuous sampling significant blurring does not occur until μ reaches $2\pi f_m$. The numerical implementation of the BKFIL algorithm introduces errors that increase with attenuation, especially errors in the back-projection operation. The exponential factor in the attenuated back-projection operator (16) goes from a constant value at $\mu = 0$ to an increasingly oscillatory function as μ increases. To numerically evaluate the back-projection integral, therefore, finer angular sampling is required as the attenuation coefficient increases. Rolling off the ramp filter dampens the aliasing artifacts that insufficient angular and lateral sampling produce.

The statistical properties of the filtering method presented here are given by simple statistical formulas for the mean, variance, %RMS uncertainty, and the covariance function of the reconstructed image. The square of %RMS uncertainty is inversely proportional to the measured counts

(88). Simulations show that the constant of proportionality is a function of filter resolution characteristics, attenuation coefficient, and size of the cross-sectional image.

Previous simulations have shown [2] that filtering methods are less precise than iterative methods, possibly because iterative methods can simultaneously make adjustments in the solution based on information from all projections, whereas convolution methods modify only one projection at a time. Filtering methods, however, are much faster and cheaper to implement.

An important application of this method of attenuation compensation is the reconstruction of radionuclide distributions such as ^{99m}Tc and ^{123}I in the brain. Simulations show that variation in attenuation coefficients between bone, gray matter, and white matter do not present serious artifacts. The BKFIL algorithm can compensate for attenuation in single-photon ECT using an attenuation-dependent filter which reconstructs the transverse section reliably. The BKFIL algorithm requires two times more computer time if $\mu > 0$ than if $\mu = 0$ due to the exponential calculation in the back-projection operation. Thus, the computer time requirements are only two times that of conventional TCT or positron ECT, and there is no increase in memory requirements.

ACKNOWLEDGMENTS

This research was supported in part by the Biology and Medicine Division of the U.S. Department of Energy (contract W-7405-ENG-48) and the National Cancer Institute (contract YO1-CB-50304). We thank Dr. Ronald Huesman for his helpful comments and suggestions, Mr. Bob Stevens for the preparation of the illustrations, and Mr. Don Mason, Jr. for some of the computer simulations.

REFERENCES

[1] T.F.Budinger and G.T.Gullberg, "Transverse section reconstruction of gamma-ray emitting radionuclides in patients," in Reconstruction Tomography in Diagnostic Radiology and Nuclear Medicine, M.M.Ter-Pogossian, M.E.Phelps, G.L.Brownell, J.R.Cox, Jr., D.O.Davis, and R.G.Evens, Eds. Baltimore: University Park Press, 1977, pp.315-342.

[2] G.T.Gullberg, "The Attenuated Radon Transform: Theory and Application in Medicine and Biology," Ph.D. Thesis, University of California, Berkeley, California, Lawrence Berkeley Laboratory Report LBL-7486, 1979.

[3] J.Radon, "Über die Bestimmung von Funktionen durch ihre integralwerte längs gewisser Mannigfaltigkeiten," Ber. Saechs. Akad. Wiss. Leipzig, Math.-Phys. Kl., vol. 69, pp.262-277, 1917.

[4] R.N.Bracewell and A.C.Riddle, "Inversion of fan-beam scans in radio astronomy," Astrophysics J., vol. 150, pp.427-434, 1967.

[5] G.N.Ramachandran and A.V.Lakshminarayanan, "Three-dimensional reconstruction from radiographs and electron micrographs: application of convolutions instead of Fourier transforms," Proc. Nat. Acad. Sci. U.S., vol. 68, pp.2236-2240, 1971 .

[6] L.A.Shepp and B.F.Logan, "The Fourier reconstruction of a head section," IEEE Trans. Nucl. Sci., vol. NS-21, pp.21-43, 1974.

[7] R.H.Huesman, G.T.Gullberg, W.L.Greenberg, and T.F.Budinger, "RECLBL Library Users Manual—Donner Algorithms for Reconstruction Tomography," Tech. Rpt. PUB-214, Lawrence Berkeley Laboratory, 1977.

[8] O.J.Tretiak and P.Delaney, "The exponential convolution algorithm for emission computed axial tomography," in Review of Information Processing in Medical Imaging, Proc. Fifth Internat'l Conference, Vanderbilt University, June 27 - July 1, 1977, A.B.Brill and R.R.Price, Eds., Oak Ridge National Laboratory Report ORNL/BCTIC-2, 1978, pp.266-278.

[9] O.J.Tretiak and C.Metz, "The exponential Radon transform," J. SIAM (in press, 1980).

[10] T.F.Budinger and G.T.Gullberg, "Three-dimensional reconstruction in nuclear medicine emission imaging," IEEE Trans. Nucl. Sci. vol. NS-21, pp.2-20, 1974.

[11] T.F.Budinger, G.T.Gullberg, and R.H.Huesman, "Emission computed tomograpny," in Image Reconstruction from Projections: Implementation and Applications, G.T.Herman, Ed., New York: Springer-Verlag, pp.147-246, 1979.

[12] L.T.Chang, "A method for attenuation correction in radionuclide computed tomography," IEEE Trans. Nucl. Sci., Vol. NS-25(2), pp.638-643, 1978.

[13] T.E.Walters, W.Simon, D.A.Chesler, J.A.Correia, and S.J.Riederer, "Radionuclide axial tomography with correction for internal absorption," in Information Processing in Scintigraphy, C.Raynaud and A.Todd-Pokropek, Eds., Orsay, France: Comissariat à l'energie Atomique, pp.333-342, 1976.

[14] S.Bellini, M.Piacentini, C.Cafforio, and F.Rocca, "Compensation of tissue absorption in emission tomography," IEEE Trans., Vol. ASSP-27(3), pp.213-218, 1979.

[15] S.Bellini, M.Piacentini, C.Cafforio, and F.Rocca, "Design of a computerized emission tomographic system," Signal Processing, vol. 1, pp.125-131, 1979.

[16] F.Natterer, "On the inversion of the attenuated Radon transform," Universitat des Saarlandes, Saarbrucken, Report A-78/17, 1978.

[17] G.L.Brownell, J.A.Correia, and R.G.Zamenhof, "Positron instrumentation," in Recent Advances in Nuclear Medicine, vol. V, J.H.Lawrence and T.F.Budinger, Eds., New York: Grune & Stratton, 1978, pp.1-49.

[18] M.E.Phelps, "Emission computed tomography," Seminars in Nucl. Med., vol. 7, pp.337-365, 1977.

[19] M.M.Ter-Pogossian, "Basic principles of computed axial tomography," Seminars in Nucl. Med., vol. 7, pp.109-128, 1977.

[20] R.H.T.Bates and T.M.Peters, "Towards improvements in tomography," New Zealand J. Sci., vol. 14, pp.883-896, 1971.

[21] T.F.Budinger and G.T.Gullberg, "Reconstruction by two-dimensional filtering of simple superposition transverse-section image," in Technical Digest: Image Processing for 2-D and 3-D Reconstruction from Projections: Theory and Practice in Medicine and the Physical Sciences, August 4-7, 1975, Washington, D.C.: Opt. Soc. Amer., 1975.

[22] G.T.Gullberg, "The reconstruction of fan-beam data by filtering the back-projection," Comp. Graphics and Image Processing, vol. 10, pp.30-47, 1979.

[23] E.T.Whittaker and G.N.Watson, A Course of Modern Analysis, Cambridge, England: Cambridge University Press, 4th edition, 1962.

[24] E.Tanaka and T.A.Iinuma, "Correction functions and statistical noises in transverse section picture reconstruction," Comput. Biol. Med., vol. 6, pp.295-306, 1976.

[25] K.Miller, "New results on reconstruction methods from x-ray projections," Math. 290 Lecture Notes, University of California, Berkeley, 1979.

[26] D.A.Chesler and S.J.Riederer, "Ripple suppression during reconstruction in transverse tomography," Phys. Med. Biol., vol. 20, pp.632-636, 1975.

[27] L.A.Shepp and J.B.Kruskal, "Computerized tomography: the new medical x-ray technology," Amer. Math. Monthly, vol. 85(6), pp.420-439, 1978.

[28] S.W.Rowland, "Computer implementation of image reconstruction formulas," in Image Reconstruction from Projections: Implementation and Application, G.T.Herman, Ed., New York: Springer-Verlag, 1979, pp.9-79.

[29] E.T.Tsui, "Estimation and Filtering Theory Applied to Computer Tomography in Low Dose Environments," Ph.D. Thesis, University of California, Berkeley, 1978.

[30] E.T.Tsui and T.F.Budinger, "A stochastic filter for transverse section reconstruction," IEEE Trans. Nucl. Sci., vol. NS-26(2), pp.2687-2690, 1979.

[31] R.K.Otnes and L.Enochson, Digital Time Series Analysis. New York: Wiley, 1972.

[32] R.W.Hamming, Digital Filters. Englewood Cliffs, NJ: Prentice Hall, 1977.

[33] R.N.Bracewell, The Fourier Transform and Its Applications. New York: McGraw-Hill, 1965.

[34] H.H.Barrett, S.K.Gordon, and R.S.Hershel, "Statistical limitations in transaxial tomography," Comput. Biol. Med., vol. 6, pp.307-323, 1976.

[35] C.R.Crawford and A.C.Kak, "Aliasing artifacts in computerized tomography," Applied Optics, vol. 18(21), pp.3704-3711, 1979.